Cell Reports Medicine, Volume *5*

Supplemental information

Arachidonic acid released by PIK3CA mutant tumor cells triggers malignant transformation of colonic epithelium by inducing chromatin remodeling

Baoyu He, Qingli Bie, Rou Zhao, Yugang Yan, Guanjun Dong, Baogui Zhang, Sen Wang, Wenrong Xu, Dongxing Tian, Yujun Hao, Yanhua Zhang, Mingsheng Zhao, Huabao Xiong, and Bin Zhang

Supplemental Information

Arachidonic acid released by PIK3CA mutant tumor cells triggers malignant transformation of colonic epithelium by inducing chromatin remodeling

Baoyu He[1,2,8], Qingli Bie[1,2,8], Rou Zhao[1], Yugang Yan[3], Guanjun Dong[4], Baogui Zhang[5], Sen Wang[1], Wenrong Xu[6], Dongxing Tian[1], Yujun Hao[7], Yanhua Zhang[7], Mingsheng Zhao[4], Huabao Xiong[4,*], Bin Zhang[1,9,*]

[1]Department of Laboratory Medicine, Affiliated Hospital of Jining Medical University, Jining Medical University, Jining, Shandong 272000, China

[2]School of Integrative Medicine, Shandong University of Traditional Chinese Medicine, Jinan, Shandong 250355, China

[3]school of medical engineering, Jining Medical University, Jining, Shandong 272067, China

[4]Institute of Immunology and Molecular Medicine, Jining Medical University, Jining, Shandong 272067, China

[5]Department of Gastrointestinal Surgery, Affiliated Hospital of Jining Medical University, Jining Medical University, Jining, Shandong 272000, China

[6]Key Laboratory of Laboratory Medicine of Jiangsu Province, School of Medicine, Jiangsu University, Zhenjiang, Jiangsu 212000, China

[7]State Key Laboratory of Oncogenes and Related Genes, Shanghai Cancer Institute, Renji Hospital, Shanghai Jiao Tong University School of Medicine, Shanghai 200032, China

[8]These authors contributed equally

[9]Lead contact

[#]Correspondence: zhangbin@mail.jnmc.edu.cn (B.Z.), xionghbl@163.com (H.X.)

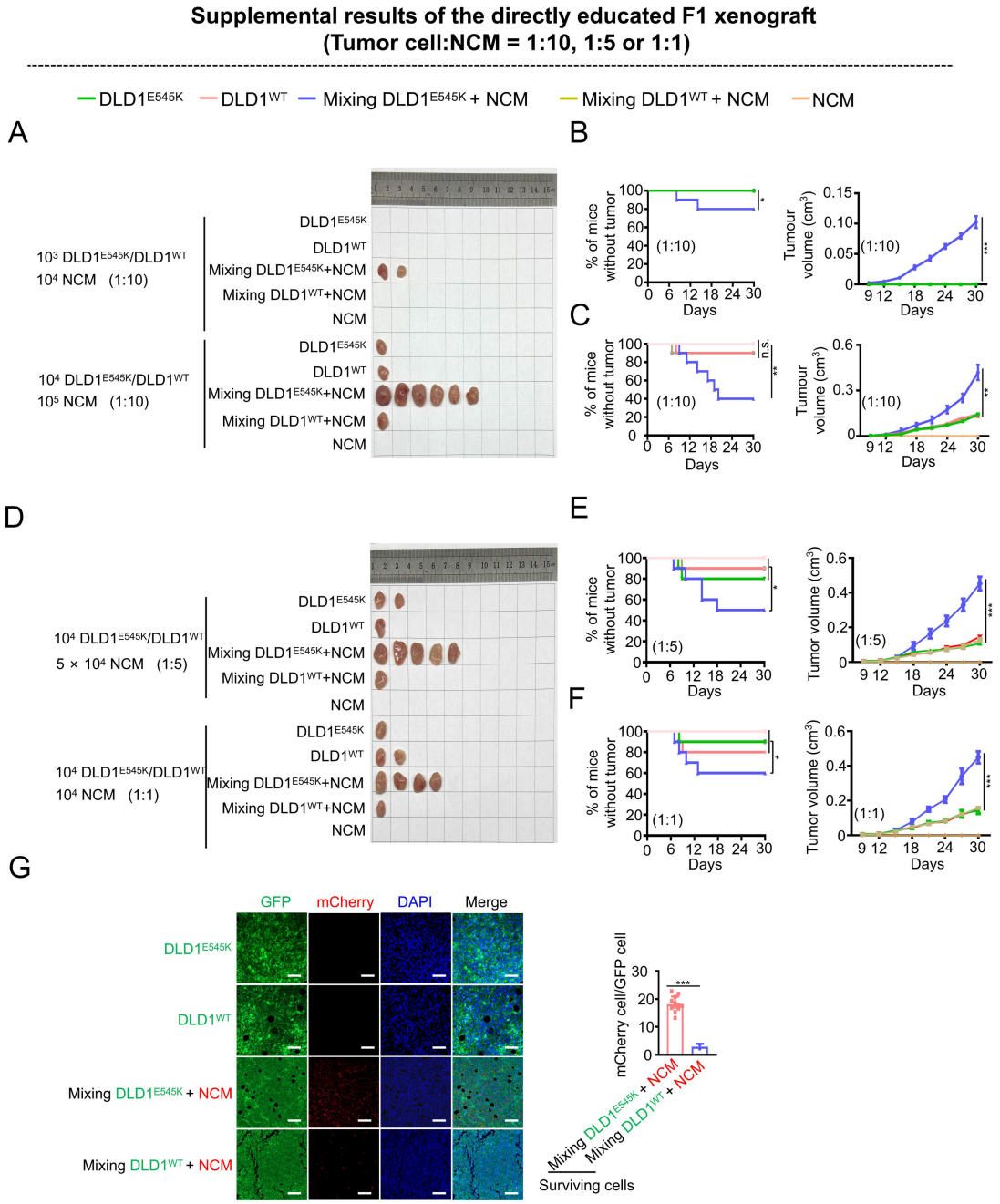

Supplemental Figure 1: Supplemental results of the Direct Education Model involving PIK3CA E545K mutant tumor cells and NCM460 cells (related to Fig. 1).

(A) Photographs of tumors established using the indicated cells of the Direct Education F1 Xenograft. The ratio of tumor cell and NCM460 cell is 1:10.

(B and C) Tumor incidence and tumor volume of the Direct Education F1 xenograft of S1A (n=10). In the left panel of B section, the plotted lines of DLD1^{E545K} group, DLD1^{WT} group, Mixing DLD1^{WT} + NCM group, and NCM group were overlapped. B

and C: data are represented as means ± SEM; n = 10 mice per cohort.

(D) Photographs of tumors established using the indicated cells of the Direct Education F1 Xenograft. The ratio of tumor cell and NCM460 cell is 1:5 (upper) or 1:1 (bottom)..

(E and F) Tumor incidence and tumor volume of the Direct Education F1 Xenograft. of S1C. E and F: data are represented as means ± SEM; n = 10 mice per cohort.

(G) The indicated xenograft tissues were stained with anti-GFP (representing PIK3CA E545K mutant cells or PIK3CA WT cells) and anti-mCherry (representing NCM460 cells) antibodies, and the ratio of $mCherry^{+}$ cells to GFP^{+} cells in the F1 xenograft was quantified. Scale bar = 20 μm. Data are represented as means ± SEM; n = 12 mice per cohort.

Statistical analyses, n.s., not significant; $^{*}p < 0.05$; $^{**}p < 0.01$; $^{***}p < 0.001$. P-values in (B, left), (C, left), (E, left) and (F, left) were calculated with two-way ANOVA test. P-values in (B, right), (C, right), (E, right) and (F, right) were calculated using log-rank test. P-values in (G, right) were calculated using two-tailed student's t-test.

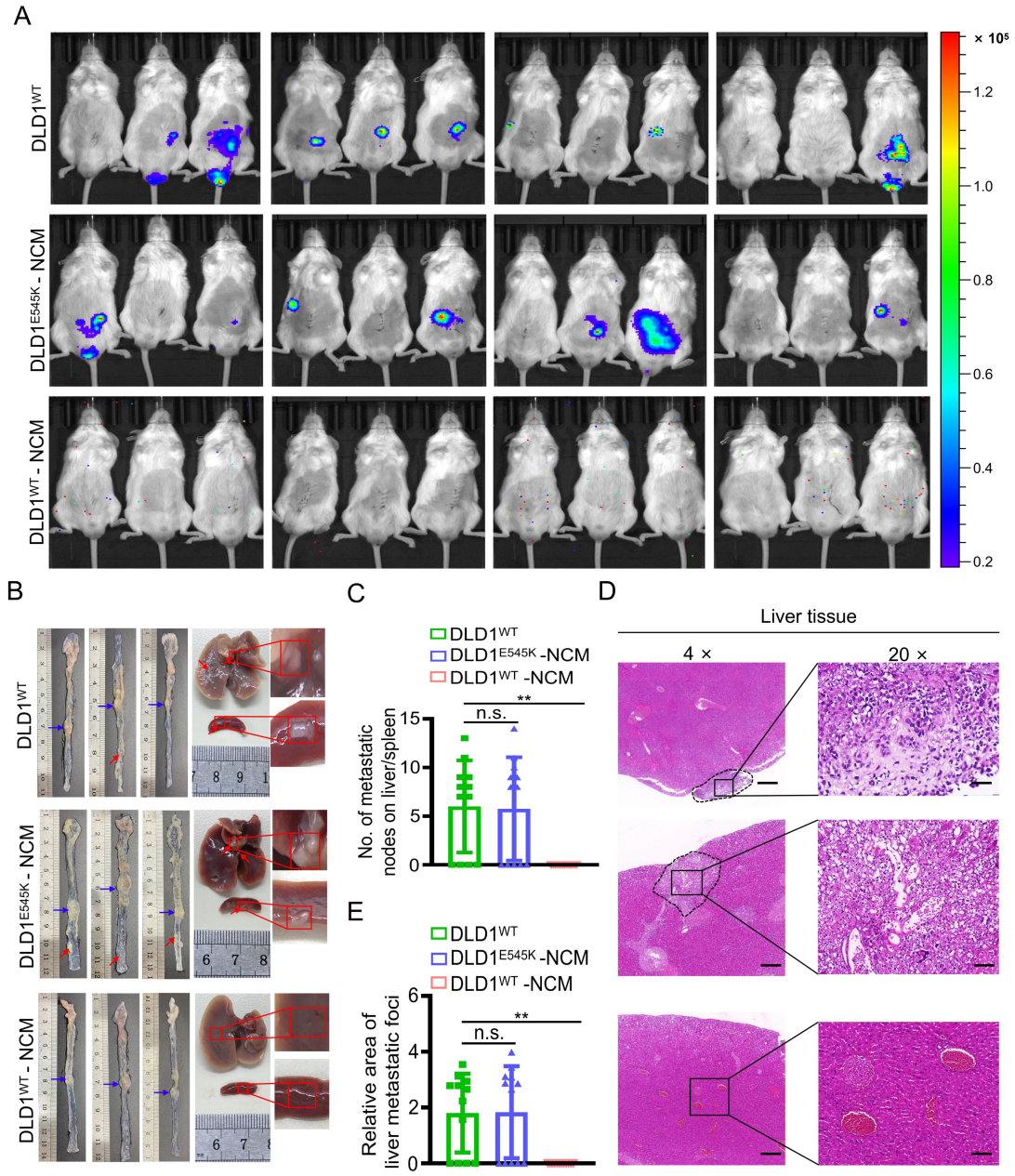

Supplemental Figure 2: Supplemental results of the colon orthotopic tumor metastasis model established using the directly educated-NCM460 F2 cells (related to Fig. 1).

(A) Representative bioluminescent images of mice from the colon orthotopic metastasis model.

(B) Representative macroscopic images of the colon, liver, and spleen from the colon orthotopic metastasis model. The blue arrow indicates the inoculation site in the distal colon, and the red arrow indicates metastatic nodules in the rectum, liver and spleen.

(C) Numbers of metastasized tumor nodules in the liver and spleen per mouse were

counted (mean ± SEM, n = 12 mice per cohort).

(D) Representative H&E images of the liver tissues from the colon orthotopic metastasis model. We can clearly see the metastatic lesions on the liver tissues from the colon orthotopic metastasis model established by $DLD1^{E545K}$ tumor cell educated-NCM460 F2 cells. 4×: scale bar = 1000 μm; 20×: scale bar = 20 μm.

(E) Relative areas of metastatic foci in the liver were calculated (mean ± SEM, n = 12 mice per cohort).

Statistical analyses, n.s., not significant; **p < 0.01; P-values in (C) and (E) were calculated using two-tailed student's t-test.

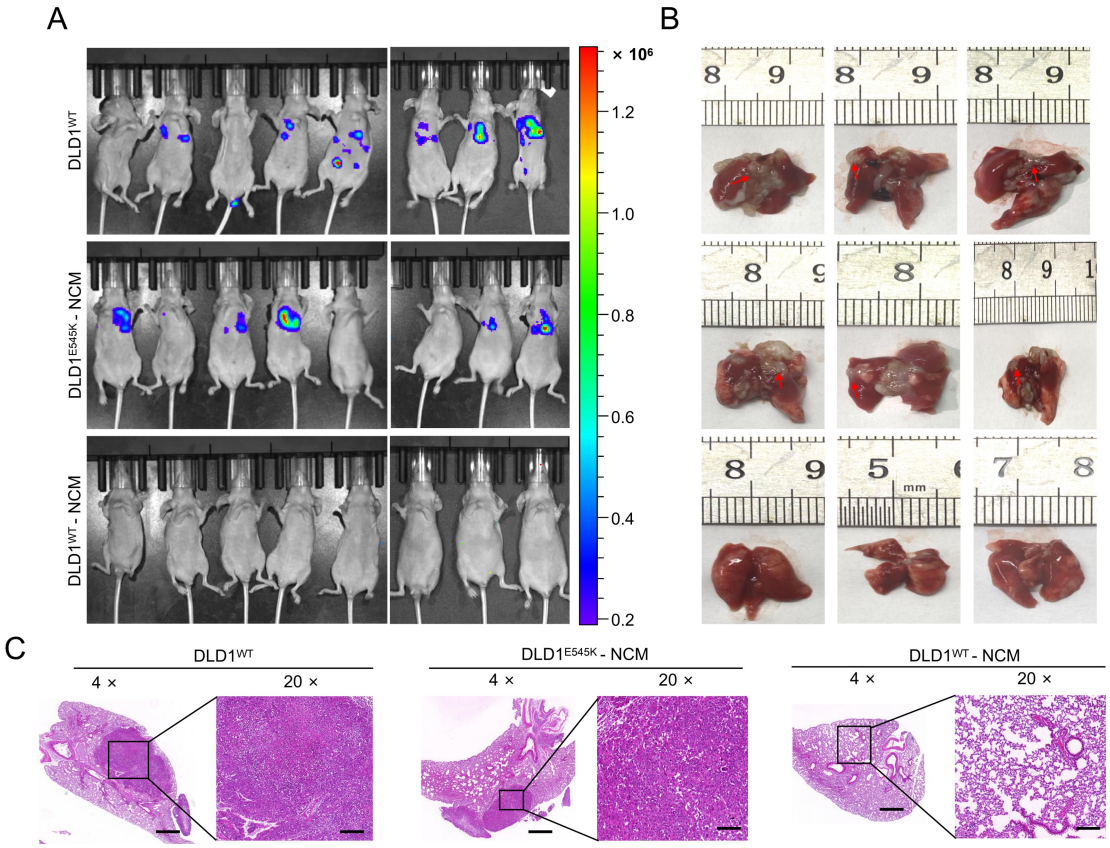

Supplemental Figure 3: Supplemental results of the tail vein metastasis model established using the directly educated-NCM460 F2 cells (related to Fig. 1).

(A) Representative bioluminescent images of mice in the tail vein metastasis model..

(B) Representative lung images in the tail vein metastasis model.

(C) Representative H&E staining on tumor lung foci in nude mice. 4×: scale bar = 1000 μm; 20×: scale bar = 20 μm.

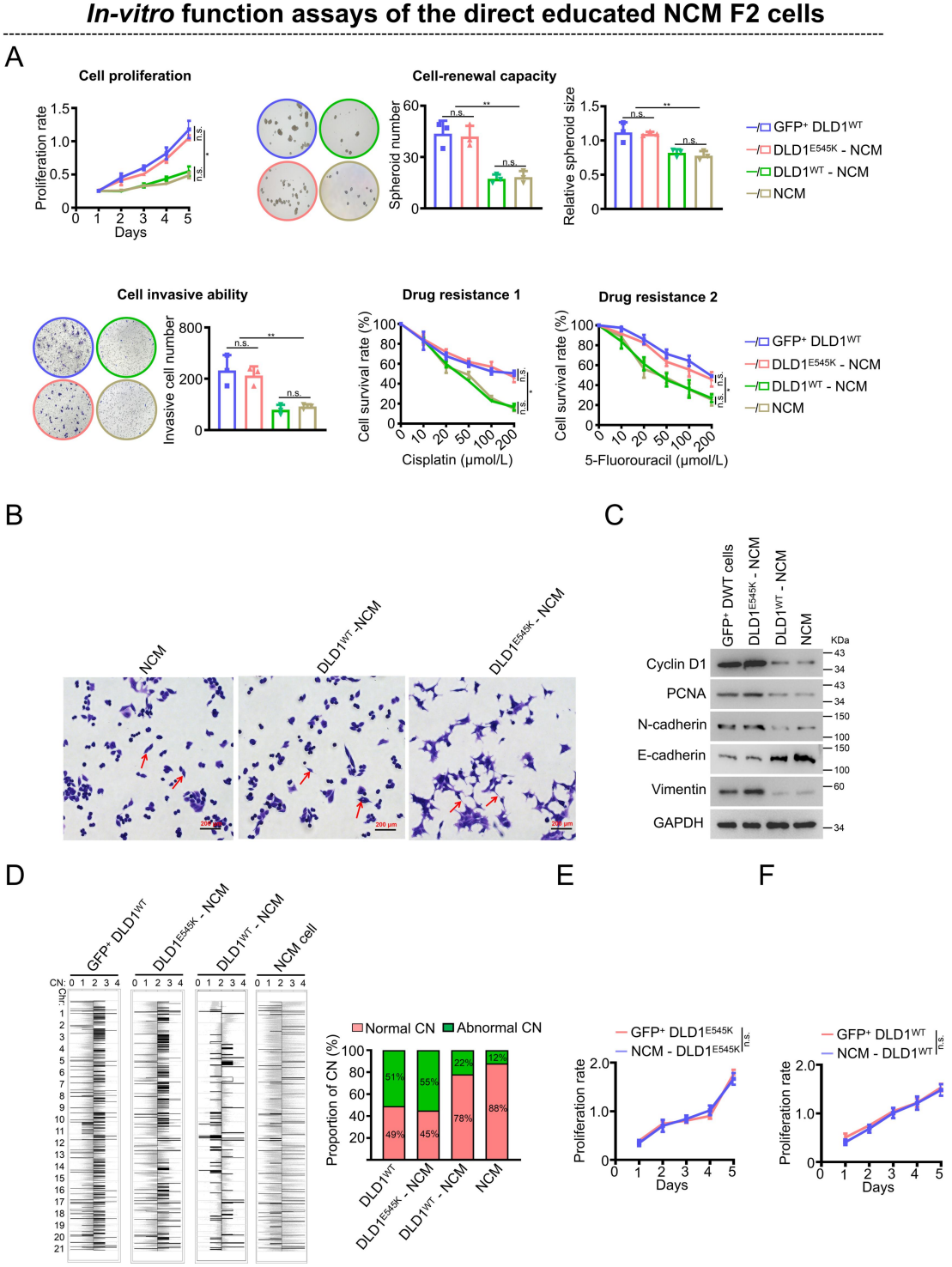

Supplemental Figure 4: Supplemental results of the Direct Education Model involving PIK3CA E545K mutant tumor cells and NCM460 cells (related to Fig. 1).

(A) *In-vitro* function of NCM460 F2 cells sorted from the directly educated xenograft tumors was assayed, including cell viability, cell renewal capacity, cell invasive ability, and sensitivity to cisplatin and 5-fluorouracil (mean ± SEM, n = 3 biological

replicates).

(B) Representative morphological images of NCM460 F2 cells sorted from the directly educated xenograft tumors, as assessed by phase contrast microscopy (100 ×). Crystal violet was used for cells staining.

(C) Assessment of EMT-related markers, including N-cadherin, E-cadherin, and Vimentin, in NCM460 F2 cells sorted from the directly educated xenograft tumors.

(D) Copy Number Variation Analysis (CNV) based on whole-genome sequencing was performed on $DLD1^{WT}$ cells, NCM460 F2 cells sorted from the directly educated xenograft tumors, and the NCM460 cell line.

(E) Assessment of cell viability in sorted $DLD1^{E545K}$ cells from xenografts established using "pure $DLD1^{E545K}$ cells" and "cell mixture of $DLD1^{E545K}$ and NCM460" (mean ± SEM, n = 3 biological replicates).

(F) Assessment of cell viability in sorted $DLD1^{WT}$ cells from xenografts established using "pure $DLD1^{WT}$ cells" and "cell mixture of $DLD1^{WT}$ and NCM460" (mean ± SEM, n = 3 biological replicates).

Statistical analyses, n.s., not significant; $^{*}p < 0.05$; $^{**}p < 0.01$; P-values in (A) were calculated using two-way ANOVA or two-tailed student's t-test. P-values in (D) and (E) were calculated using two-way ANOVA test.

Supplemental results of the directly ducated xenograft (Tumor cell:NCM = 1:10)

A

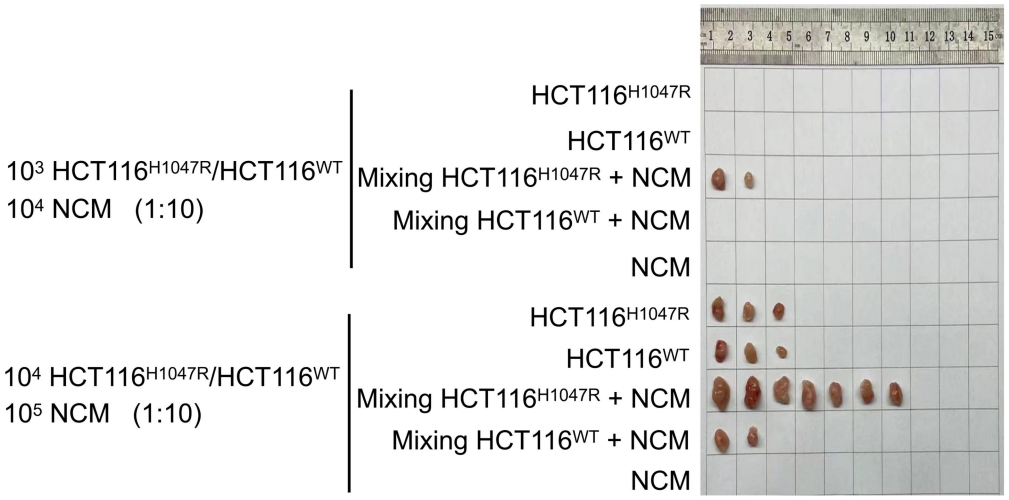

B

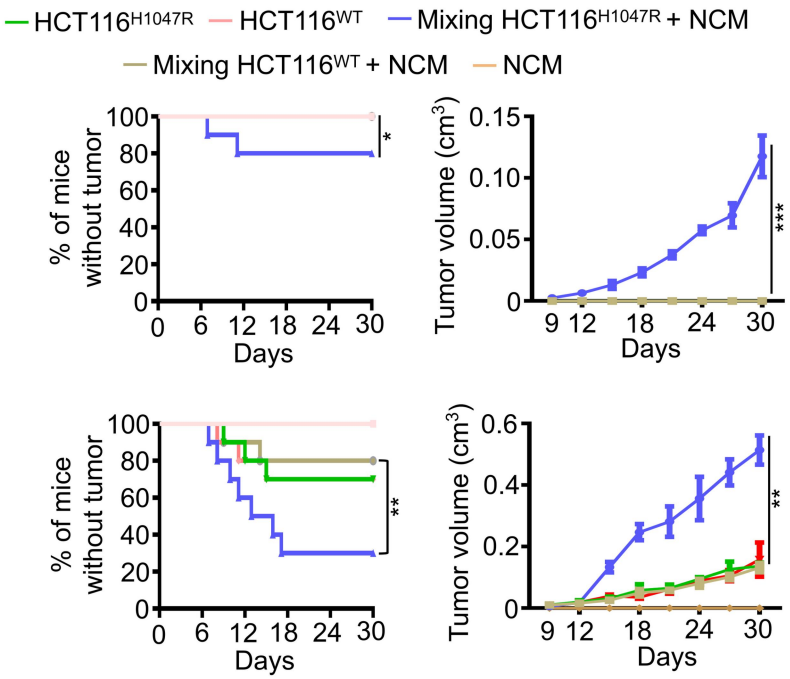

Supplemental Figure 5: Supplemental results of the Direct Education Model involving PIK3CA H1047R mutant tumor cells and NCM460 cells (related to Fig. 1).

(A) Photographs of tumors established using the indicated cells in the Direct Education F1 Xenograft. The ratio of tumor cell and NCM460 cell is 1:10.

(B) Tumor incidence and tumor volume of the Direct Education F1 Xenograft of S5A.

In the upper panel, the plotted lines of $HCT116^{H1047R}$ group, $HCT116^{WT}$ group, Mixing $HCT116^{WT}$ + NCM group, and NCM group were overlapped. Data are represented as means ± SEM; n = 10 mice per cohort.

Statistical analyses, $^{*}p < 0.05$; $^{**}p < 0.01$. P-values in (B, left) were calculated using log-rank test. P-values in (B, right) were calculated using two-way ANOVA test.

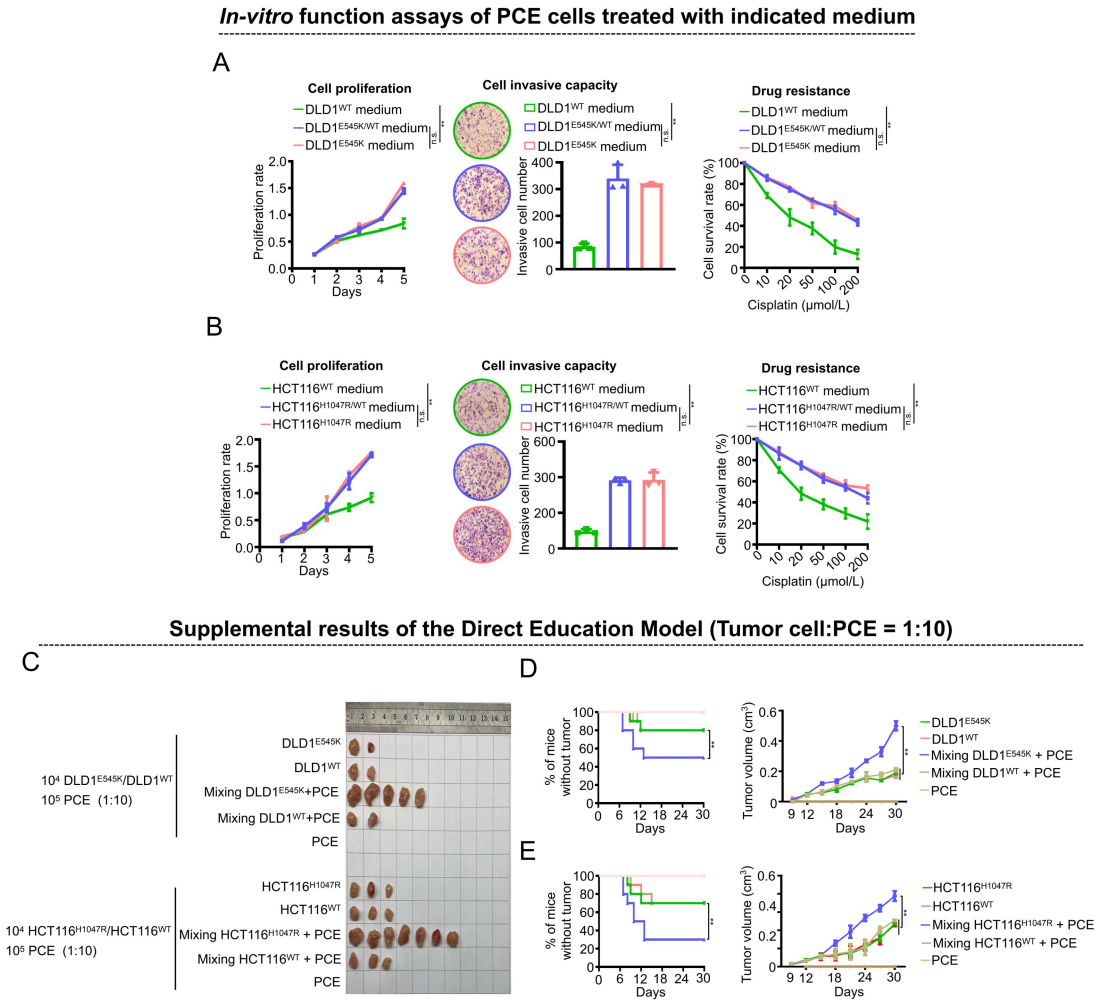

Supplemental Figure 6: *In-vitro* and *in-vivo* function assays confirming that PIK3CA mutant cells enhance cell proliferation, cell invasion, drug resistance, and tumor-forming capacity of PCE cells (related to Fig. 1).

(A and B) *In-vitro* function including cell viability, cell invasive ability, and cisplatin sensitivity of PCE cells treated with the indicated media was assayed. A and B: data are represented as means ± SEM; n = 3 biological replicates.

(C) Photographs of tumors established using the indicated cells in the Direct Education F1 Xenograft. The ratio of tumor cell and NCM460 cell is 1:10.

(D and E) Tumor incidence and tumor volume of the Direct Education F1 Xenograft of S6C. D and E: data are represented as means ± SEM; n = 10 mice per cohort.

Statistical analyses, n.s., not significant; $^{*}p < 0.05$; $^{**}p < 0.01$. P-values in (A) and (B) were calculated using two-way ANOVA or two-tailed student's t-test. p values in (D, left) and (E, left) were calculated using log-rank test. P-values in (D, right) and (E, right) were calculated using two-way ANOVA test.

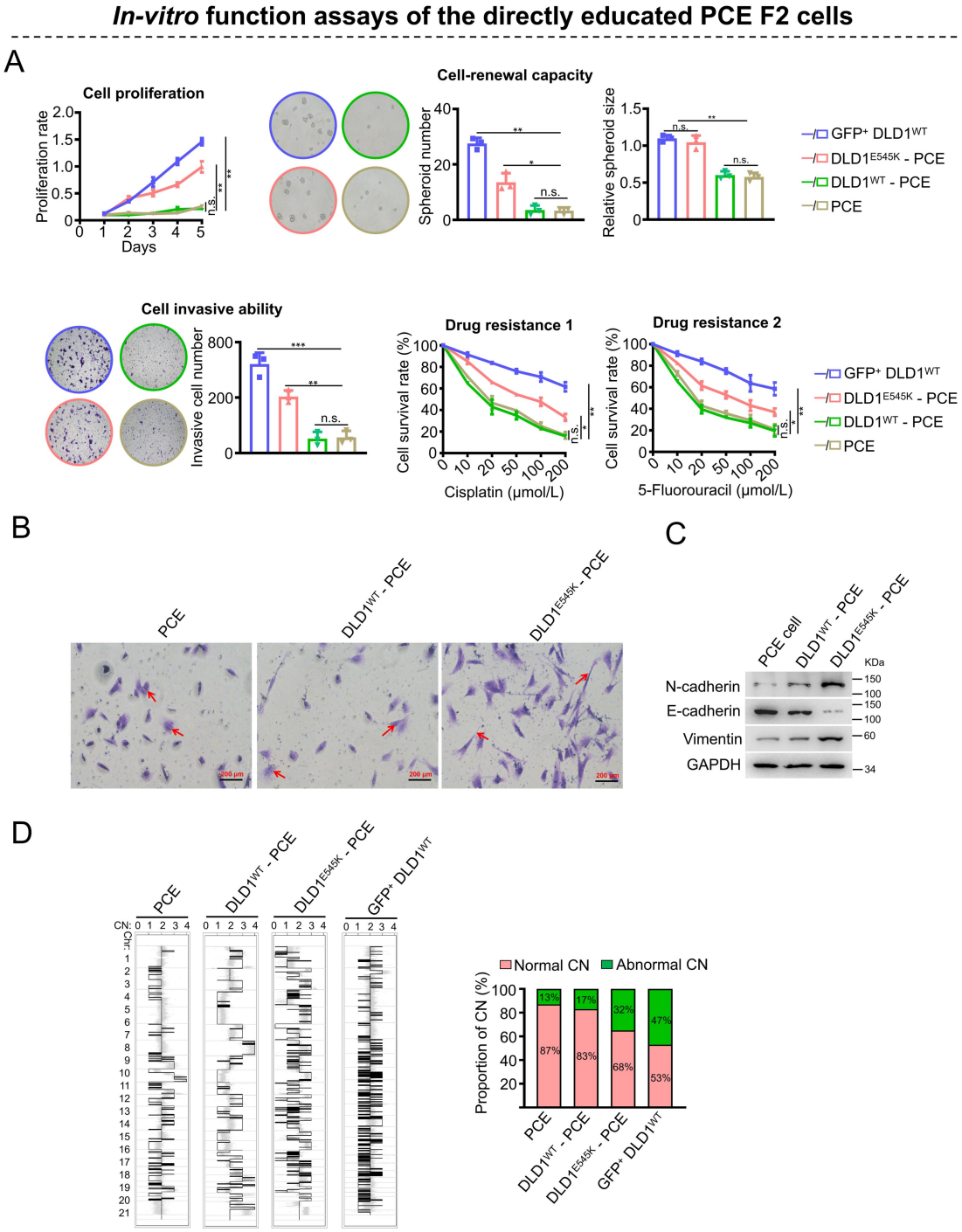

Supplemental Figure 7: Supplemental results of the Direct Education Model involving PIK3CA E545K mutant tumor cells and PCE cells (related to Fig. 1).

(A) *In-vitro* function of NCM460 F2 cells sorted from the directly educated xenograft tumors was assayed, including cell viability, cell renewal capacity, cell invasive ability, and sensitivity to cisplatin and 5-fluorouracil (mean ± SEM, n = 3 biological replicates).

(B) Representative morphological images of PCE F2 cells sorted from the directly

educated xenograft tumors, as assessed by phase contrast microscopy (100 ×). Crystal violet was used for cells staining.

(C) Assessment of EMT-related markers, including N-cadherin, E-cadherin, and Vimentin in PCE F2 cells sorted from the direct education xenograft tumors.

(D) Copy Number Variation (CNV) analysis based on whole-genome sequencing of PCE F2 cells sorted from the direct education xenograft tumors.

Statistical analyses, n.s., not significant; $^{*}p < 0.05$; $^{**}p < 0.01$; $^{**}p < 0.001$. P-values in (A) were calculated using two-way ANOVA test or two-tailed student's t-test.

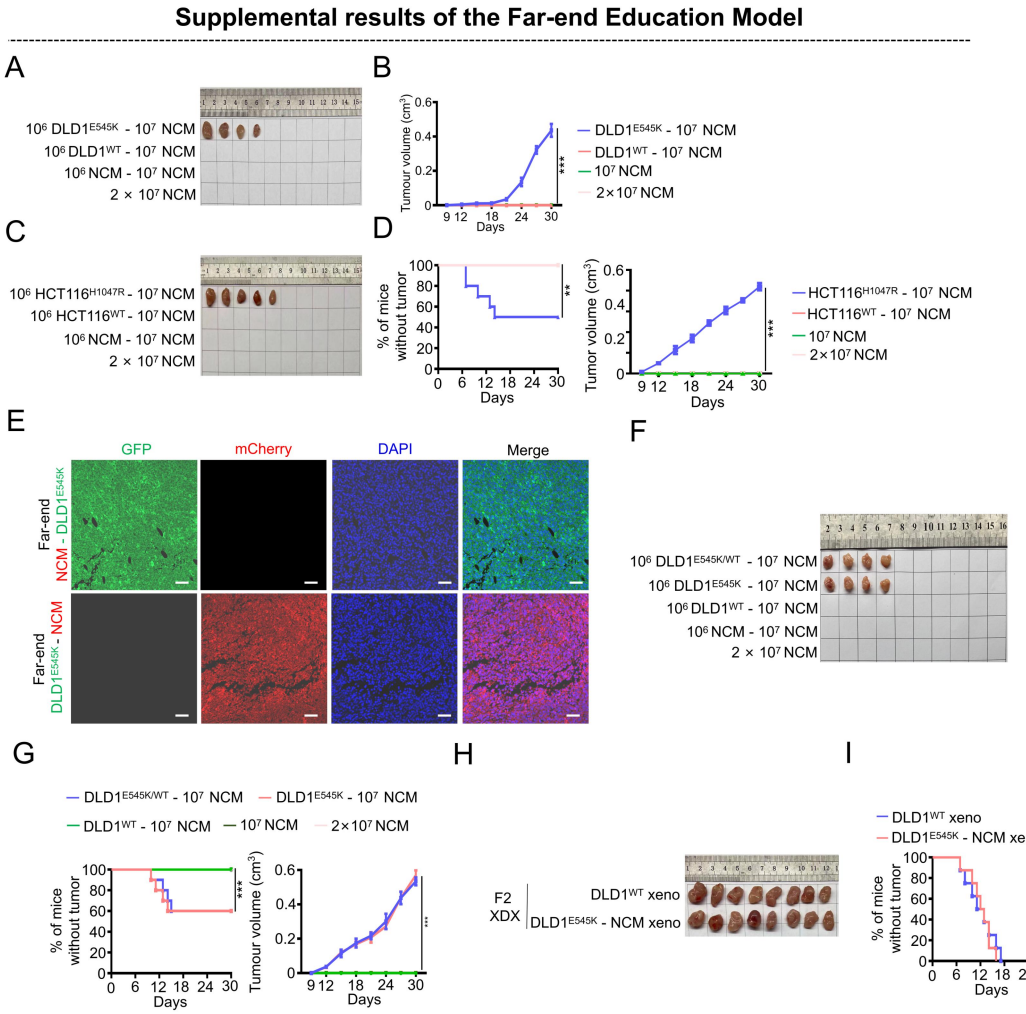

Supplemental Figure 8: Supplemental results of the Far-end Education Model involving PIK3CA E545K or H1047R mutant tumor cells and NCM460 cells (related to Fig. 1).

(A) Photographs of tumors established using the indicated cells in the Far-end Education Model.

(B) Tumor volume of NCM460 F1 xenograft from the Far-end Education Model (mean ± SEM, n = 10 mice per cohort). The plotted lines of $DLD1^{WT}$-10^7 NCM group, 10^7 NCM group and 2×10^7 NCM group were overlapped.

(C) Photographs of tumors established using the indicated cells in the Far-end Education Model.

(D) Tumor incidence and tumor volume of NCM460 F1 xenograft from the Far-end Education Model (mean ± SEM, n = 10 mice per cohort). The plotted lines of $HCT116^{WT}$-10^7 NCM group, 10^7 NCM group and 2×10^7 NCM group were

overlapped.

(E) Immunofluorescent staining of the indicated xenograft tissues using anti-GFP and anti-mCherry antibodies in the Far-end Education Model. Scale bar = 20 μm.

(F) Photographs of tumors established using the indicated cells in the Far-end Education Model.

(G) Tumor incidence and tumor volume of NCM460 F1 xenograft from the Far-end Education Model (means ± SEM, n = 10 mice per cohort). The plotted lines of $DLD1^{WT}$-10^7 NCM group, 10^7 NCM group and 2×10^7 NCM group were overlapped.

(H) Photographs of F2 XDX tumors established using the indicated xenografts from the Far-end Education Model.

(I) Tumor incidence of F2 xenofraft derived xenograft (XDX) tumors established using the indicated xenografts from the Far-end Education Model (n = 8 mice per cohort).

Statistical analyses, n.s., not significant; $^{**}p < 0.01$; $^{***}p < 0.001$. P-values in (B) and (D, right) were calculated using two-way ANOVA test. P-values in (D, left) and (G) were calculated using log-rank test.

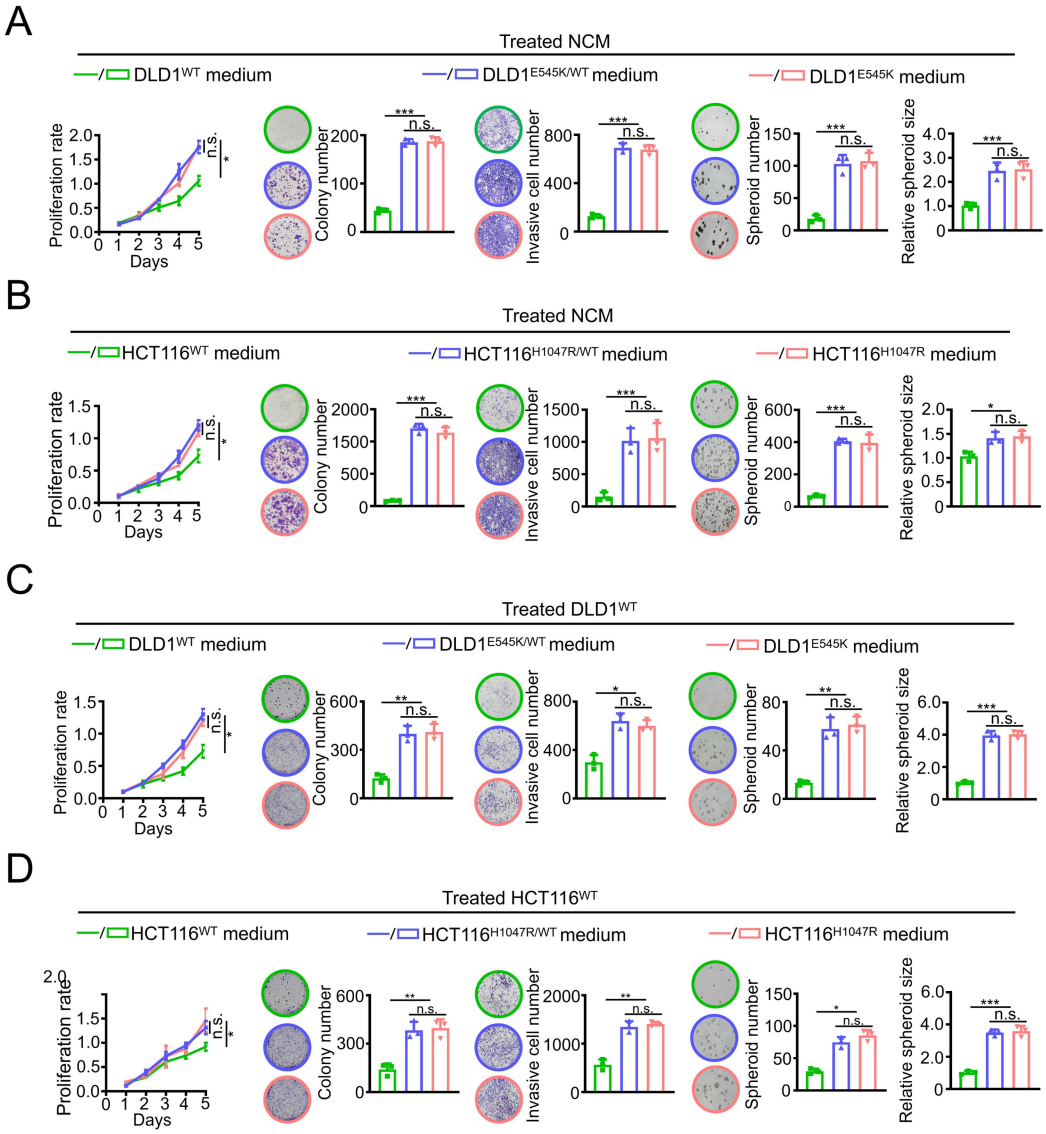

Supplemental Figure 9: *In vitro* function assays confirming that media from PIK3CA mutant cells enhances cell proliferation, clone formation, cell invasion, and self-renewal capacity of colon epithelial NCM460 cells, DLD1^{WT} cells and HCT116^{WT} cells (related to Fig. 1).

(A-D) *In-vitro* function of NCM460 cells (A and B), DLD1^{WT} cells (C) and HCT116^{WT} cells (D) treated with the indicated media was assayed, including cell viability, colony-forming efficiency, cell invasive ability, and cell renewal capacity. A-D: data are represented as means ± SEM; n = 3 biological replicates.

Statistical analyses, n.s., not significant; $^{*}p < 0.05$; $^{**}p < 0.01$; $^{***}p < 0.001$. P-values in (A), (B), (C) and (D) were calculated using two-way ANOVA test or two-tailed student's t-test.

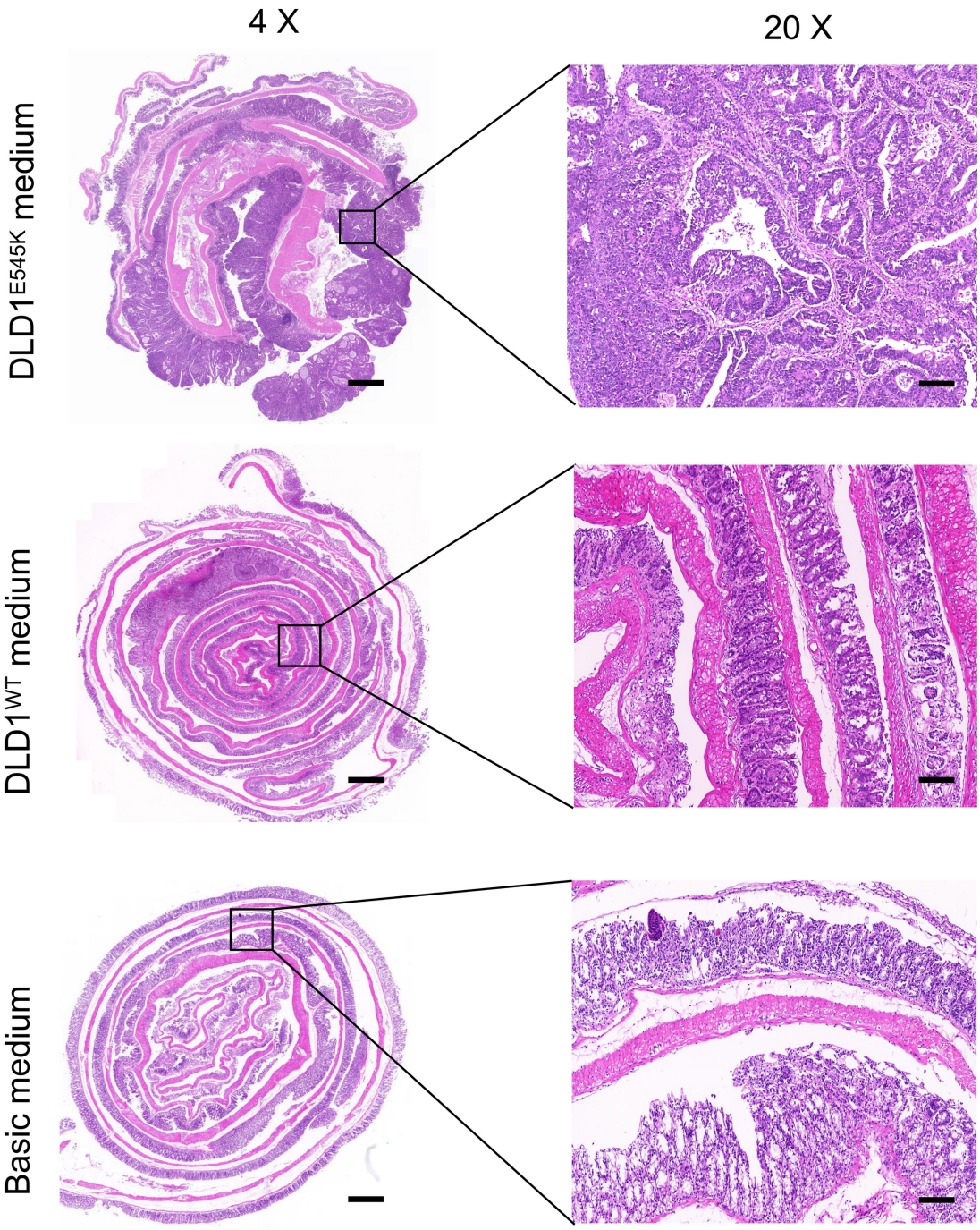

Supplemental Figure 10: Supplemental results of the AOM/DSS-induced colon tumorigenesis model (related to Fig. 1).

Representative H&E images of colon Swiss rolls from the AOM/DSS-induced colon tumorigenesis model treated with the indicated media. 4×: scale bar = 1000 μm; 20×: scale bar = 20 μm.

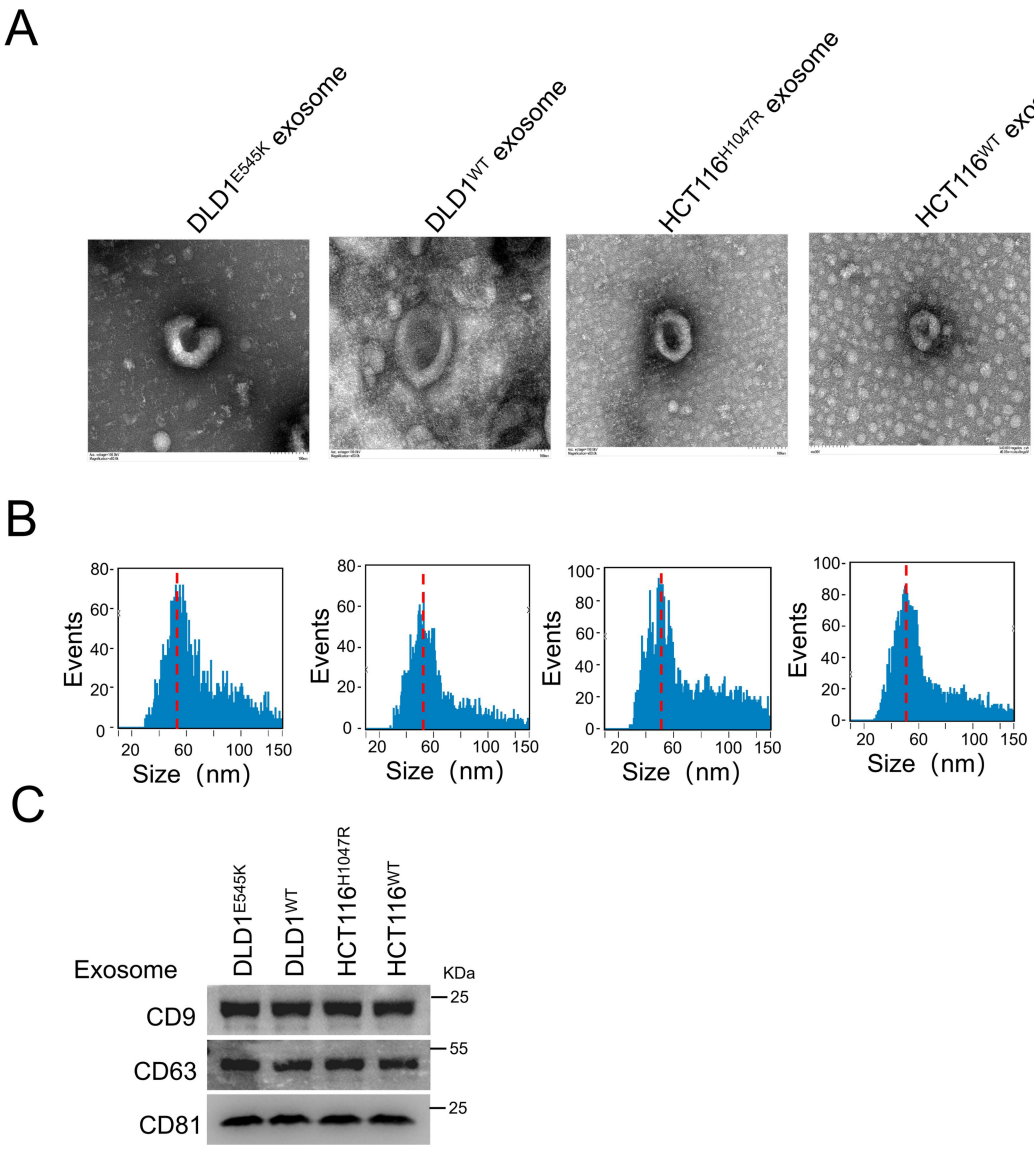

Supplemental Figure 11: Extraction and identification of exosomes (related to Fig. 2).

(A) Representative high-resolution transmission electron microscopy images of exosomes (scale bar = 100 nm).

(B) Analysis of exosome particle size using Nanosight.

(C) Detection of exosomal biomarkers (CD63, CD9 and CD81) by Western blotting analyses.

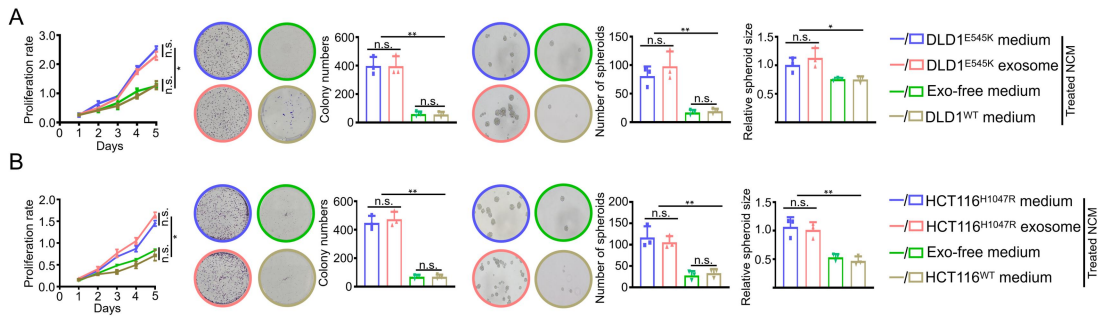

Supplemental Figure 12: *In-vitro* identification of exosomes as key mediators transmitting oncogenic mutation signals (related to Fig. 2).

(A and B) *In-vitro* function including cell viability, colony-forming efficiency, cell invasive ability, and cell renewal capacity of NCM460 cells treated with the indicated media or exosomes was assayed. A and B: data are represented as means ± SEM; n = 3 biological replicates.

Statistical analyses, n.s., not significant; $^{*}p < 0.05$; $^{**}p < 0.01$. P-values in (A) and (B) were calculated using two-way ANOVA test or two-tailed student's t-test.

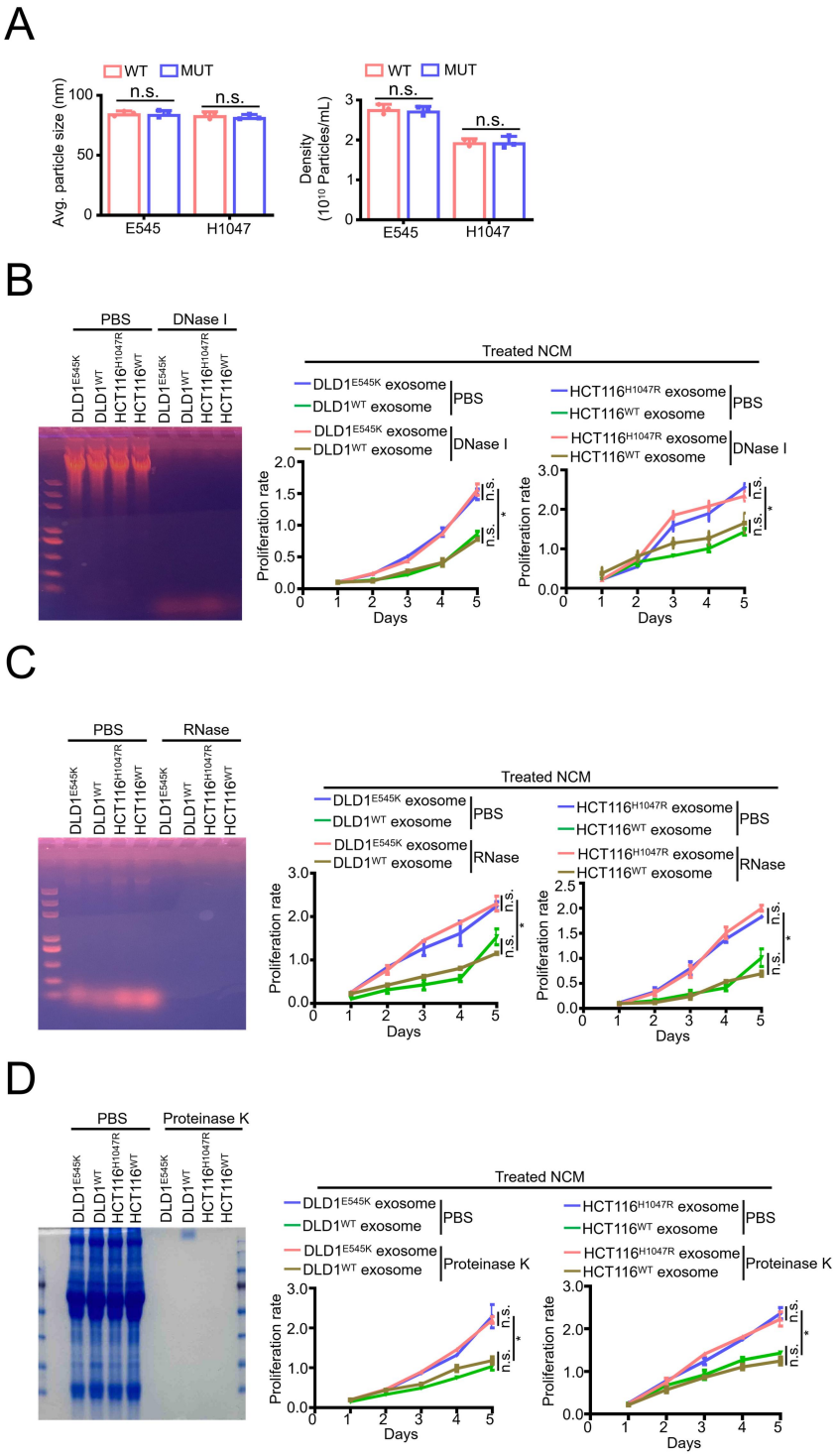

Supplemental Figure 13: The impact of DNase I, RNase, and protease K on the exosome function in transmitting oncogenic mutation signals (related to Fig. 3).

(A) Analysis and comparison of the particle sizes and densities of exosomes derived from PIK3CA mutant and isogenic WT tumor cells (means ± SEM, n = 3 biological replicates).

(B-D) Assessment of cell viability in NCM460 cells treated with exosomes pre-treated

with DNase I, RNase, or protease K. Exosomes were treated using DNase I, RNase, or protease K as described in the method section. Then, NCM460 cells were treated with hydrolysate and subjected to cell viability assay (Right panel of B-D). To verify the efficiency of enzymatic hydrolysis, total DNA, RNA or protein were extracted from treated-exosomes and subjected to agarose gel electrophoresis (total DNA or RNA) and Coomassie Blue Staining (total protein) (Left panel of B-D). Data are represented as means ± SEM; n = 3 biological replicates for proliferation assay. Statistical analyses, n.s., not significant; $^{*}p < 0.05$. P-values in (A) were calculated using two-tailed student's t-test. P-values in (B, right), (C, right) and (D, right) were calculated using two-way ANOVA test. Experiments were performed three times independently.

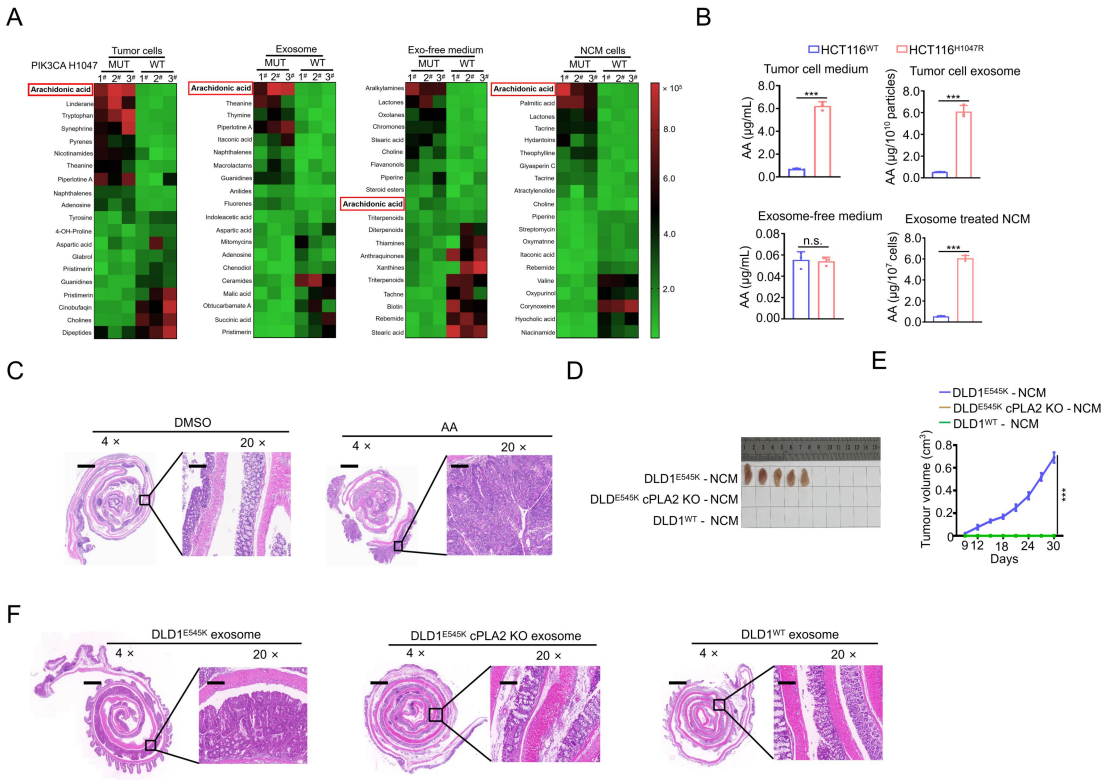

Supplemental Figure 14: Supplemental results supporting exosomal AA as the key mediator of oncogenic mutation signal transmission (related to Fig. 3).

(A) Heatmaps displaying top 20 differential metabolites (10 upregulated and 10 downregulated) in four group: PIK3CA H1047R or isogenic WT donor tumor cells, exosome components or the exosome-depleted media from the PIK3CA H1047R or isogenic WT donor tumor cells, and NCM460 recipient cells treated with exosome components from the PIK3CA H1047 or isogenic WT cells, as analyzed by untargeted metabolomics analysis (n = 3 biological replicates).

(B) Quantitative abundance of AA in medium, exosomes, and exosome-free medium derived from PIK3CA H1047R and isogenic WT cells, as well as in exosome-treated recipient NCM460 cells was measured using LC-MS/MS method (mean ± SEM, n = 3 biological replicates).

(C) Representative H&E staining images of colon swiss rolls from the AOM/DSS-induced colon tumorigenesis model treated with either DMSO or AA. 4×: scale bar = 1000 μm; 20×: scale bar = 20 μm.

(D) Photographed tumors established using the indicated cells of the Far-end Education Model; tumor cell:NCM460 cell ratio = 1:10.

(E) Tumor volume of NCM460 F1 xenografts from the Far-end Education Model. The plotted lines of DLD1^{E545K} cPLA2 KO-NCM group and DLD1^{WT} -NCM group were overlapped (means ± SEM, n = 10 mice per cohort).

(F) Representative H&E staining images of colon swiss rolls from the AOM/DSS-induced colon tumorigenesis model treated with indicated exosomes. 4×: scale bar = 1000 μm; 20×: scale bar = 20 μm.

Statistical analyses, n.s., not significant; $^{***}p < 0.001$. P-values in (B) were calculated with two-tailed student's t-test. P-values in (E) were tested with two-way ANOVA.

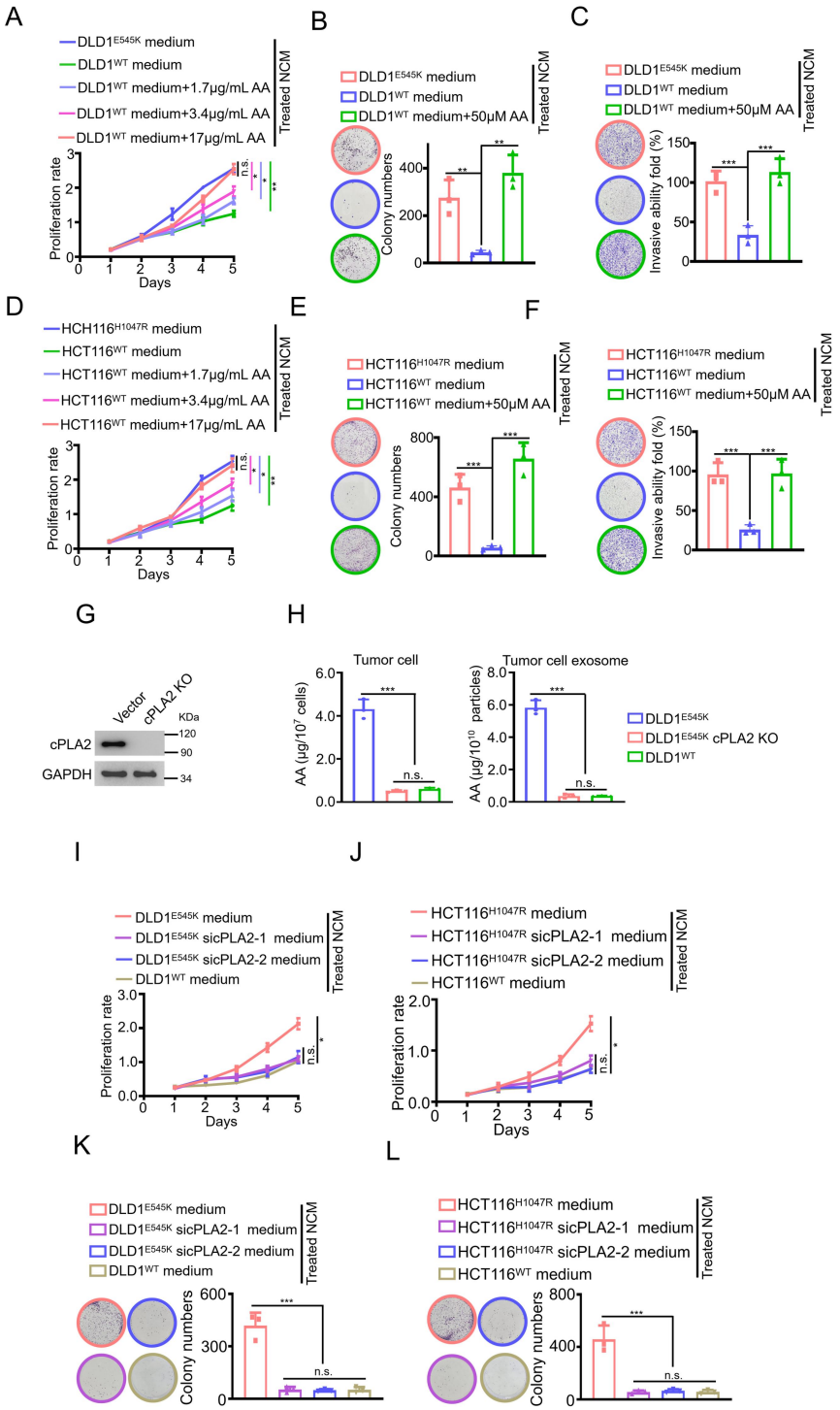

Supplemental Figure 15: Exosome-mediated AA serves as the key mediator responsible for transmitting PIK3CA mutant signals (related to Fig. 3).

(A-F) Cell viability was assessed in NCM460 cells treated with media from PIK3CA mutant or isogenic WT cells, or media from PIK3CA WT cells supplemented with exogenous AA. A-F: data are represented as means ± SEM; n = 3 biological replicates.

(G) Western blotting confirmation of cPLA2 knock-out cells.

(H) Quantitative abundance of AA in the indicated cells and exosome components was measured using LC-MS/MS method (means ± SEM; n = 3 biological replicates).

(I-L) Cell viability and colony-forming ability of NCM460 cells treated with media from PIK3CA mutant cells, cPLA2 knock-down PIK3CA mutant cells, and PIK3CA WT cells were tested. I-L: data are represented as means ± SEM; n = 3 biological replicates.

Statistical analyses, n.s., not significant; $^{*}p < 0.05$; $^{***}p < 0.001$. P-values in (A), (D), (I) and (J) were tested with two-way ANOVA. P-values in (B), (C), (E), (F), (H), (K) and (L) were calculated with two-tailed student's t-test.

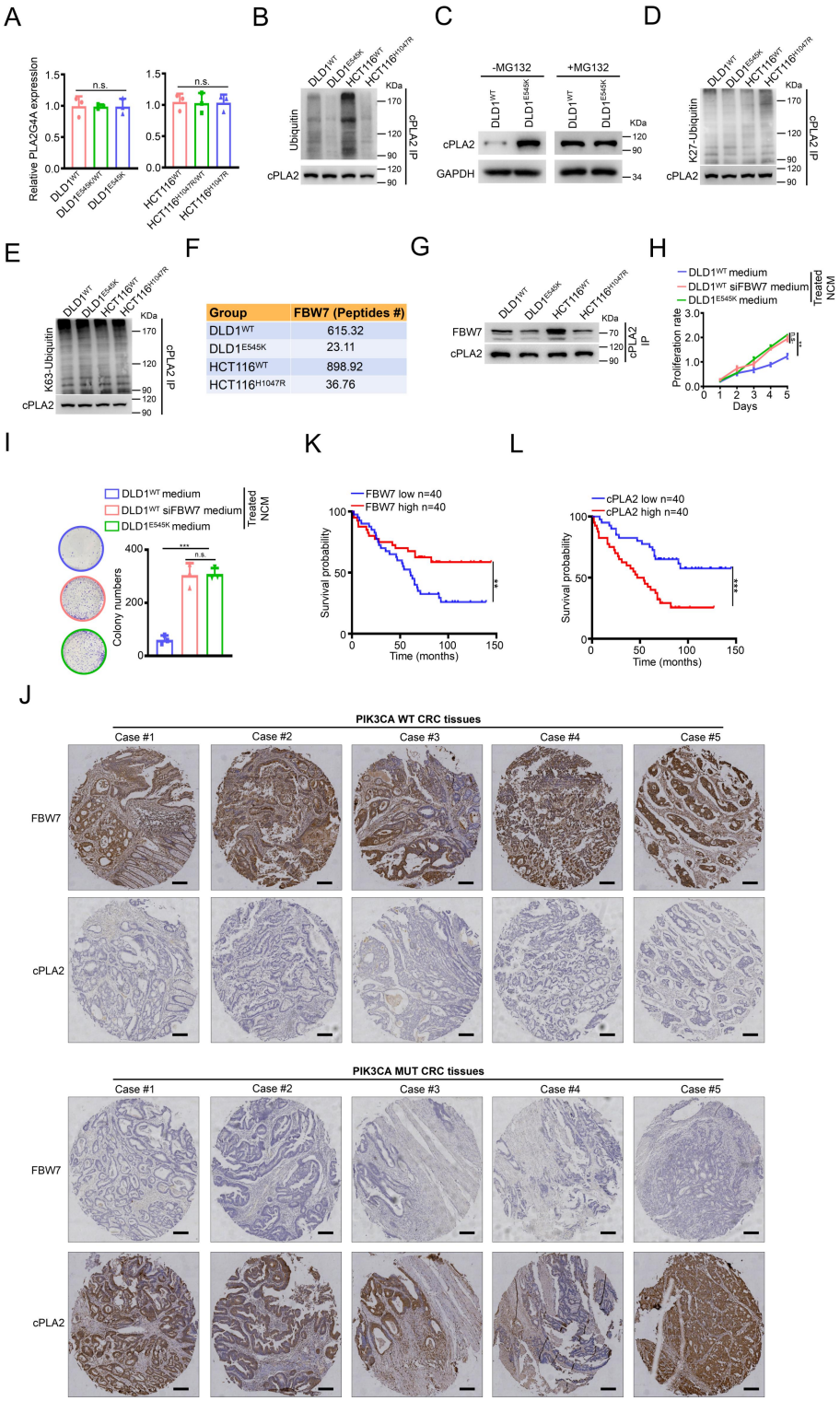

Supplemental Figure 16: Clarification of FBW7 as the E3 ubiquitin ligase of cPLA2 protein (related to Fig. 4).

(A) Expression levels of *PLA2G4A*/cPLA2 mRNA in PIK3CA mutant and isogenic WT tumor cells were measured using qPCR method (means ± SEM; n = 3 technical replicates).

(B) Cell lysates were immunoprecipitated using cPLA2 antibody in PIK3CA mutant and isogenic WT cells, followed by blotting with anti-ubiquitin to assess cPLA2 ubiquitination.

(C) $DLD1^{WT}$ cell was treated with 50 μM MG132 for 6h and then blotted with cPLA2 antibody.

(D and E) Cell lysates were immunoprecipitated using cPLA2 antibody in PIK3CA mutant and isogenic WT cells, followed by blotting with anti-K27-linked ubiquitin (D), or anti-K63-linked ubiquitin (E) antibody to assess cPLA2 ubiquitination.

(F) Analysis of differential peptides of FBW7 immunoprecipitated by cPLA2 antibody between PIK3CA mutant and isogenic WT cells using mass spectrometry.

(G) Evaluation and comparison of the interactions between cPLA2 and FBW7 in PIK3CA mutant and isogenic WT cells.

(H and I) *In-vitro* function including cell viability (H, means ± SEM, n = 3 biological replicates) and colony-forming capacity (I, means ± SEM, n = 3 biological replicates) of NCM460 cells treated with media derived from $DLD1^{WT}$ cells, $DLD1^{WT}$ FBW7 knockdown cells, and $DLD1^{E545K}$ cells was assayed.

(J) Representative IHC images of FBW7 and cPLA2 expression in PIK3CA WT (n = 67) and mutant (n = 13) CRC tissue microarray; original magnification: 40×. Scale bar = 50 μm.

(K and L) Kaplan-Meier analyses of overall survival probability of patients with tumors expressing high levels of FBW7 (or cPLA2) *vs.* low levels of FBW7 (or cPLA2).

Statistical analyses, n.s., not significant; $^{**}p < 0.01$; $^{***}p < 0.001$. P-values in (A) were calculated with two-tailed student's t-test. P-values in (H) and (I) were tested with two-way ANOVA.

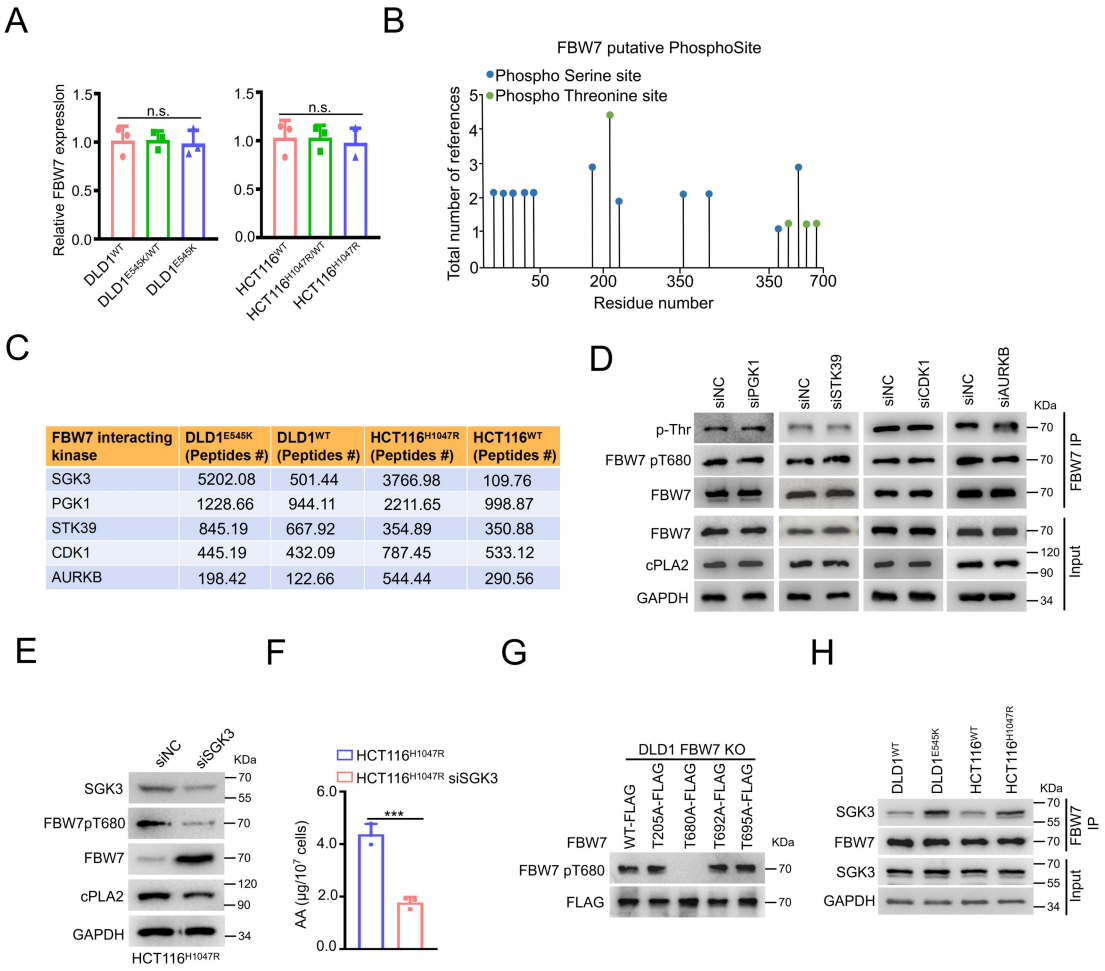

Supplemental Figure 17: Exploration of the upstream kinase of FBW7 T680 (related to Fig. 4).

(A) Measurement of FBW7 mRNA levels in PIK3CA mutant and isogenic WT cells using qPCR (means ± SEM; n = 3 technical replicates).

(B) Identification of potential phosphorylation modification sites of FBW7 obtained from the PhosphoSitePlus knowledgebase (http://www.phosphosite.org/).

(C) Analysis of differential peptides of kinases, including SGK3, PGK1, STK39, CDK1 and AURKB immunoprecipitated by anti-FBW7 antibody between PIK3CA mutant and isogenic WT cells using mass spectrometry.

(D) Scrambled siRNA (NC) or siRNAs against PGK1, STK39, CDK1 or AURKB were transfected into DLD1 parental cells for 72 h. Cell lysates were immunoprecipitated using FBW7 antibody and then blotted with the indicated antibodies.

(E and F) Scrambled siRNA (NC) or siRNAs against SGK3 were transfected into

HCT116^{H1047R} cells for 72 h. Cell lysates were blotted with the indicated antibodies (E); quantitative abundance of AA in those cells measured using LC-MS/MS method (F, means ± SEM, n = 3 biological replicates).

(G) FLAG-tagged FBW7 WT or mutant constracts including T205A, T680A, T692A and T695A, were transfected into FBW7 KO DLD1 parental cell clones. Cell lysates were blotted with the FBW7 pT680 antibody.

(H) Evaluation and comparison of the interactions between FBW7 and SGK3 in PIK3CA mutant and isogenic WT tumor cells.

Statistical analyses, n.s., not significant. P-values in (A) and (F) were calculated with two-tailed student's t-test.

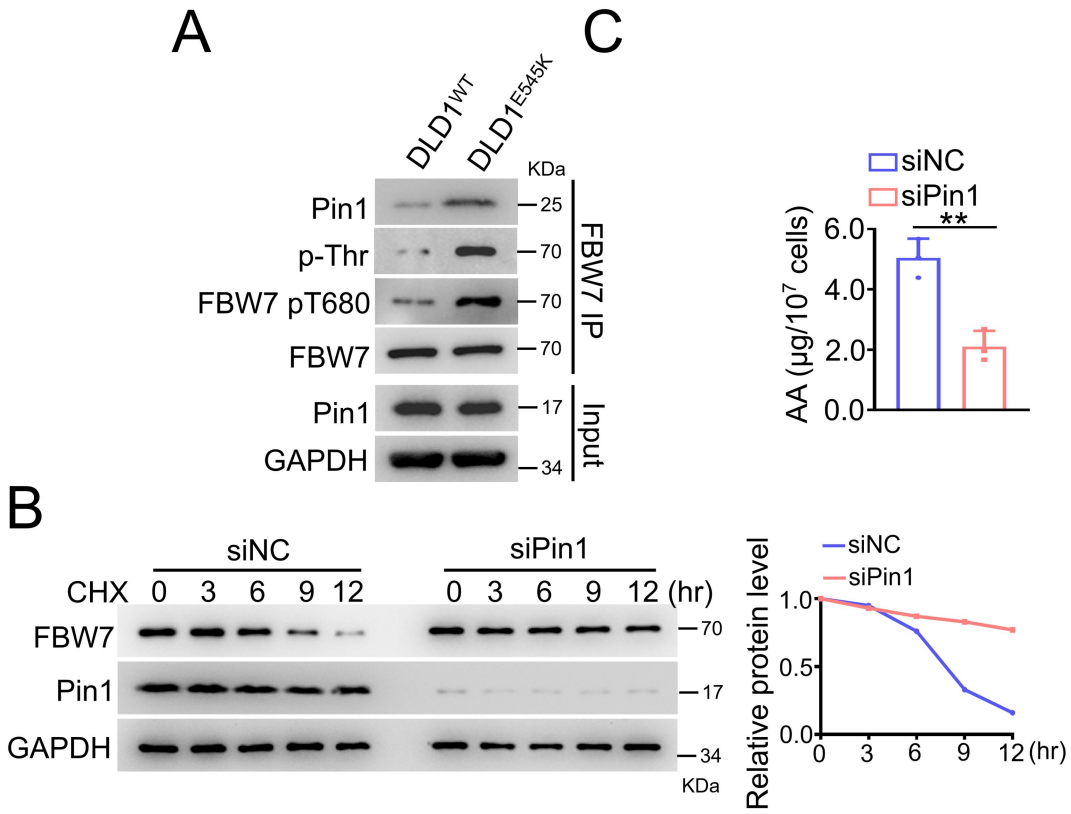

Supplemental Figure 18: Impact of PIK3CA mutation on FBW7 protein stability through the regulation of FBW7-Pin1 interaction (related to Fig. 4).

(A) Cell lysates of DLD1^{WT} and DLD1^{E545K} were immunoprecipitated with FBW7 antibody, then blotted with the indicated antibodies.

(B) DLD1^{E545K} cells were transfected with scrambled siRNA (NC) or siRNAs against Pin1. Cells were treated with 50 μM cycloheximide (CHX) for the indicated times. Cell lysates were blotted with FBW7 antibody. Western blots are shown in the left panel. Quantification of FBW7 protein levels using ImageJ is shown in the right panel.

(C) Quantitative abundance of AA in DLD1^{E545K} cells treated with scrambled siRNA (NC) or siRNAs against Pin1 was assayed using LC-MS/MS method (means ± SEM; n = 3 biological replicates).

Statistical analyses, $^{**}p < 0.01$. P-values in (A) were calculated with two-tailed student's t-test.

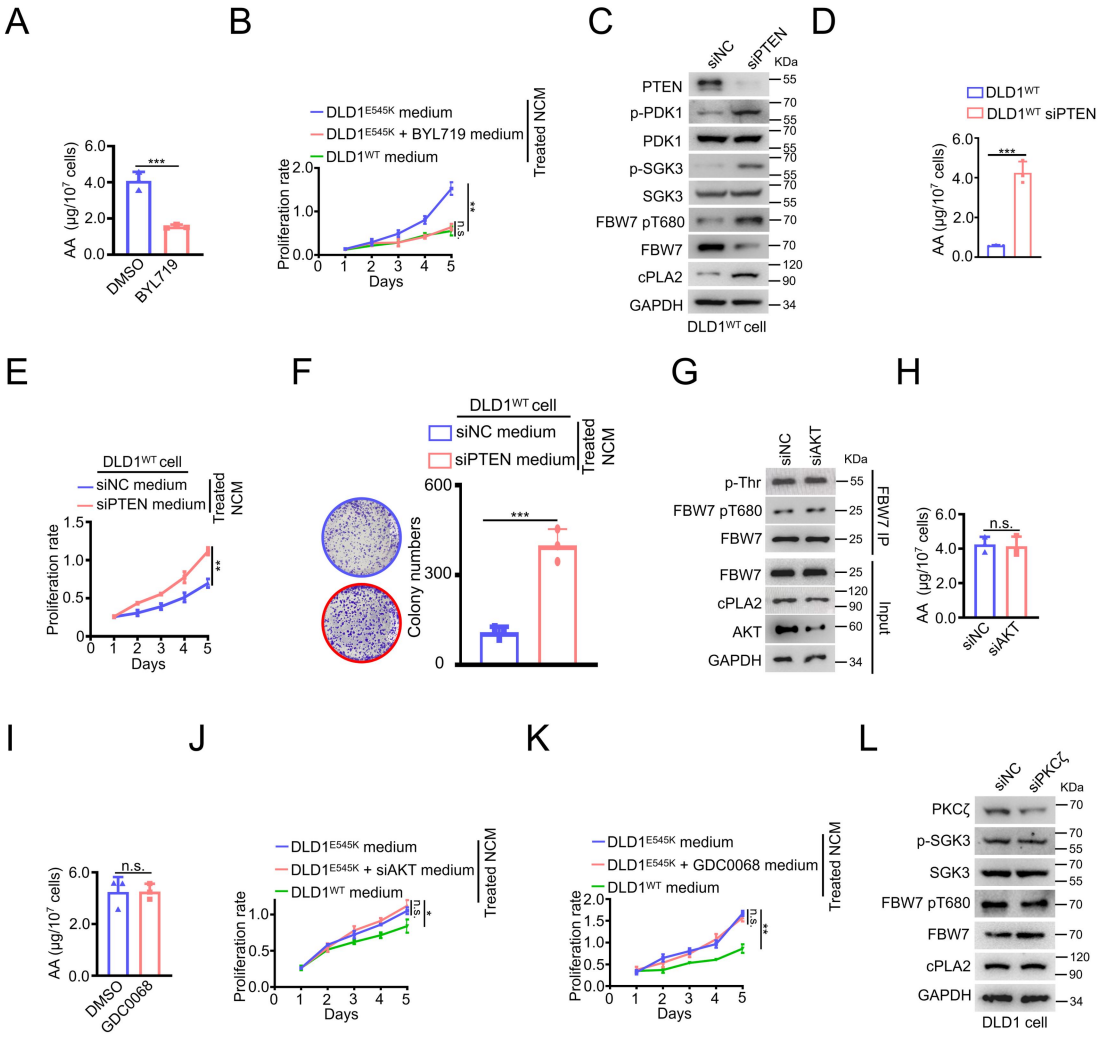

Supplemental Figure 19: PI3K-mediated FBW7 phosphorylation is independent of canonical AKT activity (related to Fig. 4).

(A) Quantitative abundance of AA in DLD1^{E545K} cells treated with DMSO or BYL719 measured using LC-MS/MS method. DLD1^{E545K} cells were treated with DMSO or 20 μM BYL719 for 48 h, and then subjected to targeted LC-MS/MS analysis (means ± SEM; n = 3 biological replicates).

(B) Cell viability of NCM460 cells treated with media from DLD1^{E545K} cells, BYL719-treated DLD1^{E545K} cells, and DLD1^{WT} cells was assayed. First, medium from DLD1^{E545K} cells, DLD1^{E545K} cells pre-treated with 20 μM BYL719 for 48 h, and DLD1^{WT} cells were obtained. Then NCM460 cells were treated with the aforesaid media and subjected to cell viability detection (means ± SEM; n = 3 biological replicates).

(C and D) Scrambled siRNA (NC) or siRNAs against PTEN were transfected into DLD1 WT cells for 72 h. Cell lysates were blotted with the indicated antibodies (C); quantitative abundance of AA in those cells measured using LC-MS/MS method (D, means ± SEM, n = 3 biological replicates).

(E and F) *In-vitro* function including cell viability (E, means ± SEM, n = 3 biological replicates) and colony-forming capacity (F, means ± SEM, n = 3 biological replicates) of NCM460 cells treated with medium derived from DLD1 WT cells and DLD1WT FBW7 knockdown cells was assayed.

(G) $DLD1^{E545K}$ cells were transfected with scrambled siRNA (siNC) or siRNAs against AKT for 72 h. Cell lysates were immunoprecipitated with FBW7 antibody, then blotted with the indicated antibodies.

(H and I) Quantitative abundance of AA in $DLD1^{E545K}$ cells treated with AKT siRNAs (H, means ± SEM, n = 3 biological replicates) or AKT inhibitor GDC0068 (I, means ± SEM, n = 3 biological replicates) was measured using LC-MS/MS method. $DLD1^{E545K}$ cells were transfected with siRNAs against AKT for 72 h, or treated with 5 μM GDC0068 inhibitor for 48 h. Then, $DLD1^{E545K}$ cells were obtained and subjected to targeted metabolic analysis.

(J and K) Cell viability of NCM460 cells treated with media from $DLD1^{E545K}$ cells, AKT siRNA (J, means ± SEM, n = 3) or AKT inhibitor GDC0068 (K, means ± SEM, n = 3) treated $DLD1^{E545K}$ cells, and $DLD1^{WT}$ cells was tested. First, media from $DLD1^{E545K}$ cells, $DLD1^{E545K}$ cells pre-treated with AKT siRNAs for 72 h, $DLD1^{E545K}$ cells pre-treated with 5 μM GDC0068 inhibitor for 48 h, and $DLD1^{WT}$ cells were obtained. Then NCM460 cells were treated with the aforesaid media and subjected to cell viability detection.

(L) Scrambled siRNA (NC) or siRNAs against PKCζ were transfected into DLD1 parental cells for 72 h. Cell lysates were blotted with the indicated antibodies.

Statistical analyses, n.s., not significant; $^{*}p < 0.05$; $^{**}p < 0.01$; $^{***}p < 0.001$. P-values in (A), (D), (F), (H) and (I) were calculated with two-tailed student's t-test. P-values in (B), (E), (G) and (K) were calculated with two-way ANOVA test.

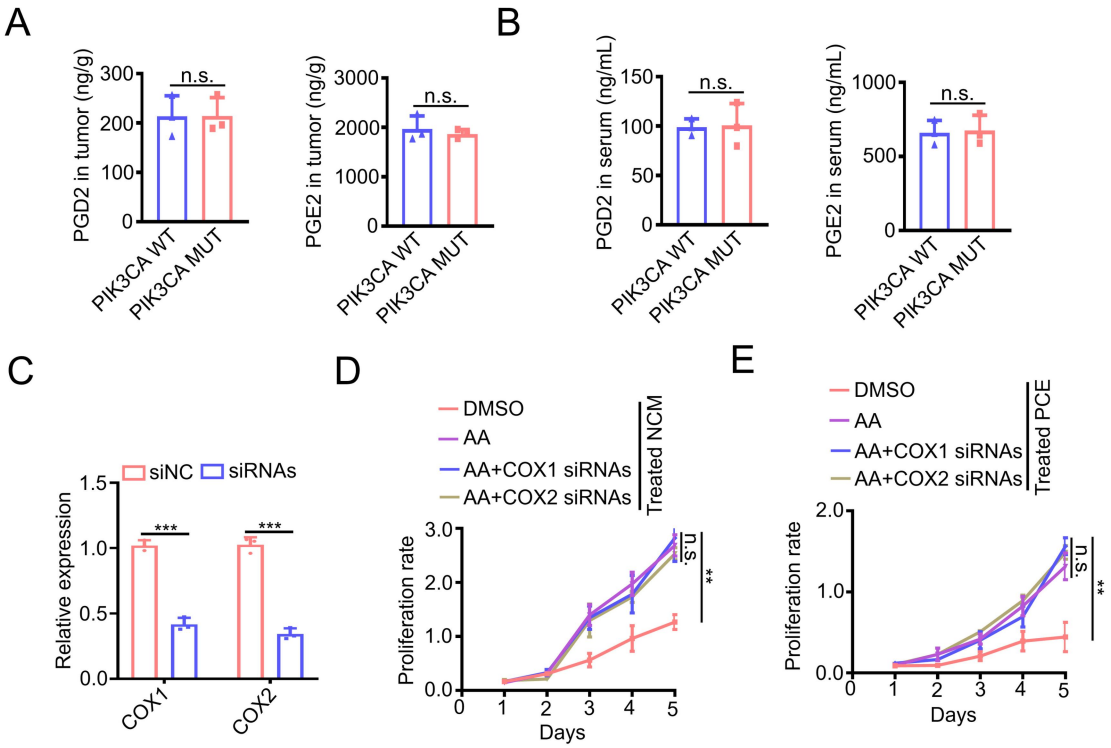

Supplemental Figure 20: Malignant phenotype of colon epithelial cells induced by AA is independent of its downstream products PGD2 and PGE2 (related to Fig. 5).

(A and B) Quantitative abundance of PGD2 and PGE2 in tumor tissues (A, means ± SEM, n = 3 biological replicates) and sera (B, means ± SEM, n = 3 biological replicates) from PIK3CA WT or mutant CRC patients was measured using LC-MS/MS method.

(C) The knock-down efficiency of COX1 and COX2 genes were evaluated using qPCR assay (means ± SEM, n = 3 technical replicates).

(D and E) Cell viability of NCM460 (D, means ± SEM, n = 3 biological replicates) and PCE cells (E, means ± SEM, n = 3 biological replicates) treated with DMSO, 10 μM AA, 10 μM AA plus COX1 siRNA, or 10 μM AA plus COX2 siRNA was assayed.

Statistical analyses, n.s., not significant; $^{**}p < 0.01$. P-values in (A) and (B) were calculated with two-tailed student's t-test. P-values in (C) and (D) were calculated with two-way ANOVA test.

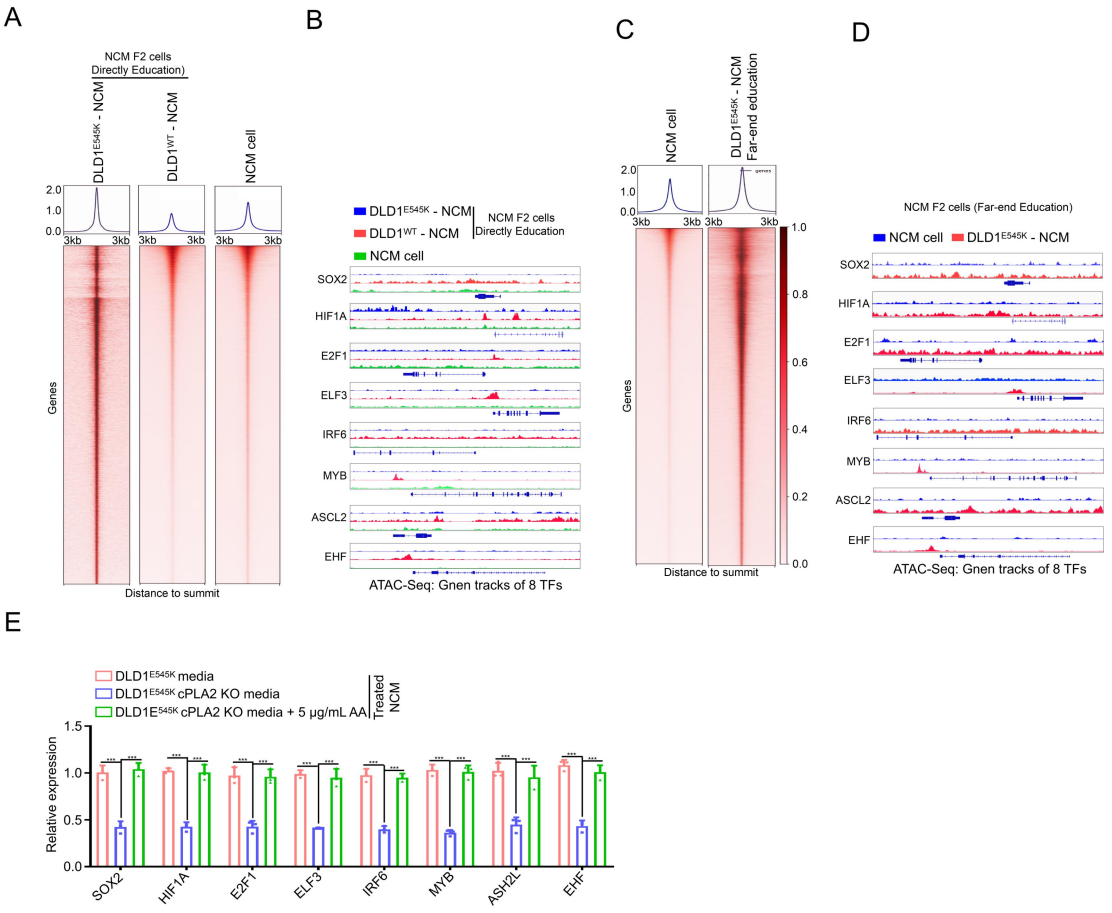

Supplemental Figure 21: Supplementary results demonstrating the impact of AA on chromatin accessibility via H3K4me3 (related to Fig. 5).

(A-D) Heatmap showing clustering of ATAC-seq data on the indicated cells from the Direct Education Model and the Far-end Education Model (A and C). Gene tracks of the 8 TFs locus with corresponding ATAC-Seq coverage files (B and D).

(E) qRT-PCR analyses of the expression of 8 TFs were performed in cell lines described above. Cell viability was assessed in NCM460 cells treated with media from DLD1^{E545K} cells, cPLA2 KO DLD1^{E545K} clones, and 5 µg/mL AA-treated cPLA2 KO DLD1^{E545K} clones (means ± SEM, n = 3 technical replicates).

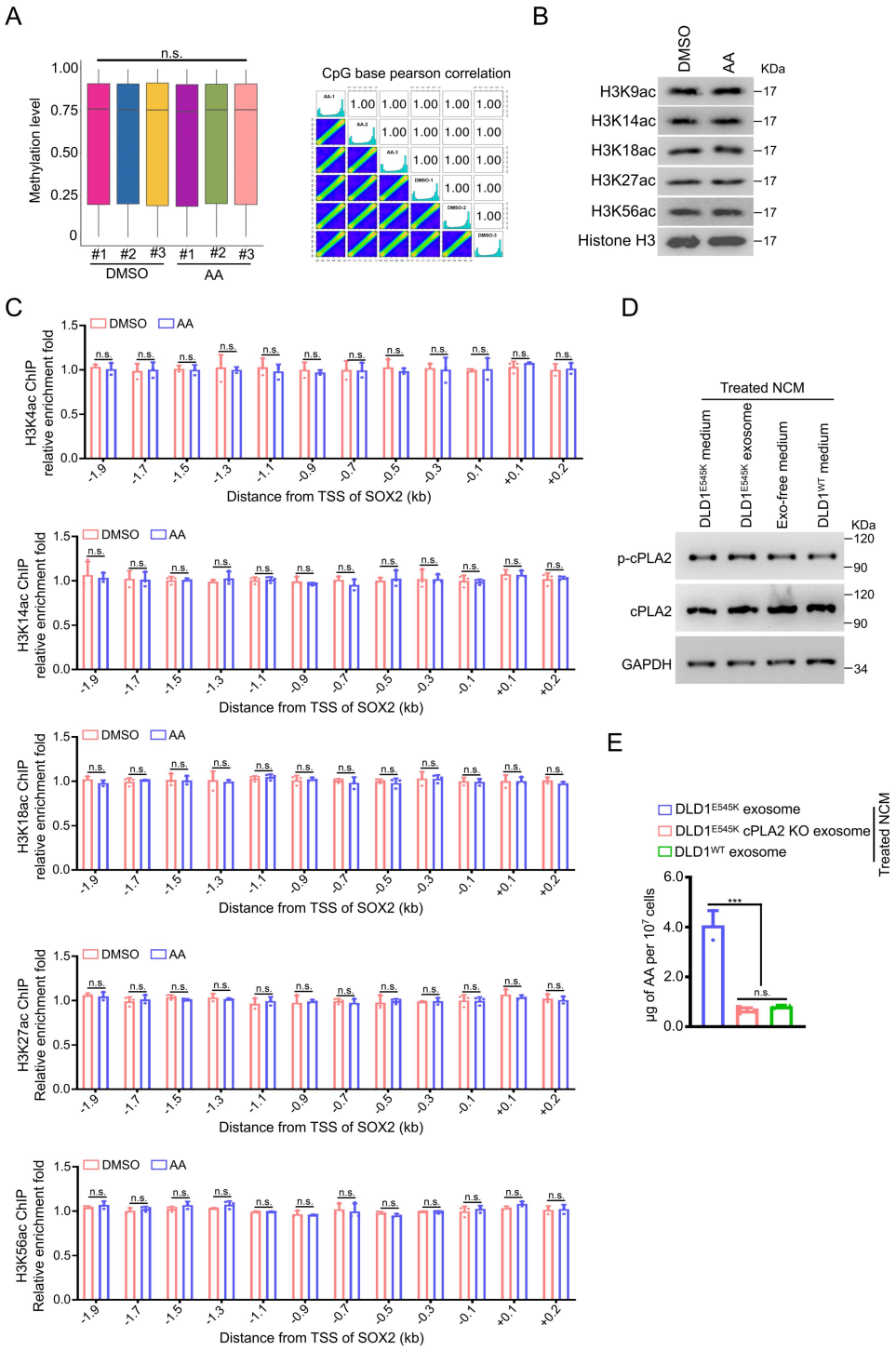

Supplemental Figure 22: AA has no significant impact on DNA methylation, histone acetylation, and cPLA2 activity in recipient NCM460 cells (related to Fig. 5).

(A) Epigenome-wide methylation profiling using Illumina Infinium MethylationEPIC BeadChip. Histogram displaying the methylation levels of NCM460 cells treated with DMSO or AA (left). Pearson's correlation analysis of the methylation levels of each

sample, with a larger coefficient indicating a higher similarity in methylation levels between the two samples (right).

(B) Immunoblot analysis of lysates from NCM460 cells treated with DMSO or AA, probed with the indicated antibodies.

(C) ChIP-PCR assays were performed in NCM460 cells treated with DMSO or AA using an anti-H3K9ac, H3K14ac, H3K18ac, H3K27ac, or H3K56ac antibodies and analyzed by quantitative PCR. Genomic DNA fragments covering +0.2 kb ~ -2.0 kb regions surrounding the transcription start site (TSS) of SOX2 were chosen (means ± SEM, n = 3 technical replicates).

(D) Evaluation of phosphorylation and total protein level of cPLA2 in NCM460 cells treated with the indicated media.

(E) Quantitative abundance of AA in NCM460 cells treated with conditioned media from the indicated cells were measured using LC-MS/MS method (means ± SEM, n = 3 biological replicates).

Statistical analyses, n.s., not significant; $^{***}p < 0.001$. P-values in (A, left) and (O) were calculated with two-tailed student's t-test. P-values in (A, right) were tested with spearman rank-correlation analysis.

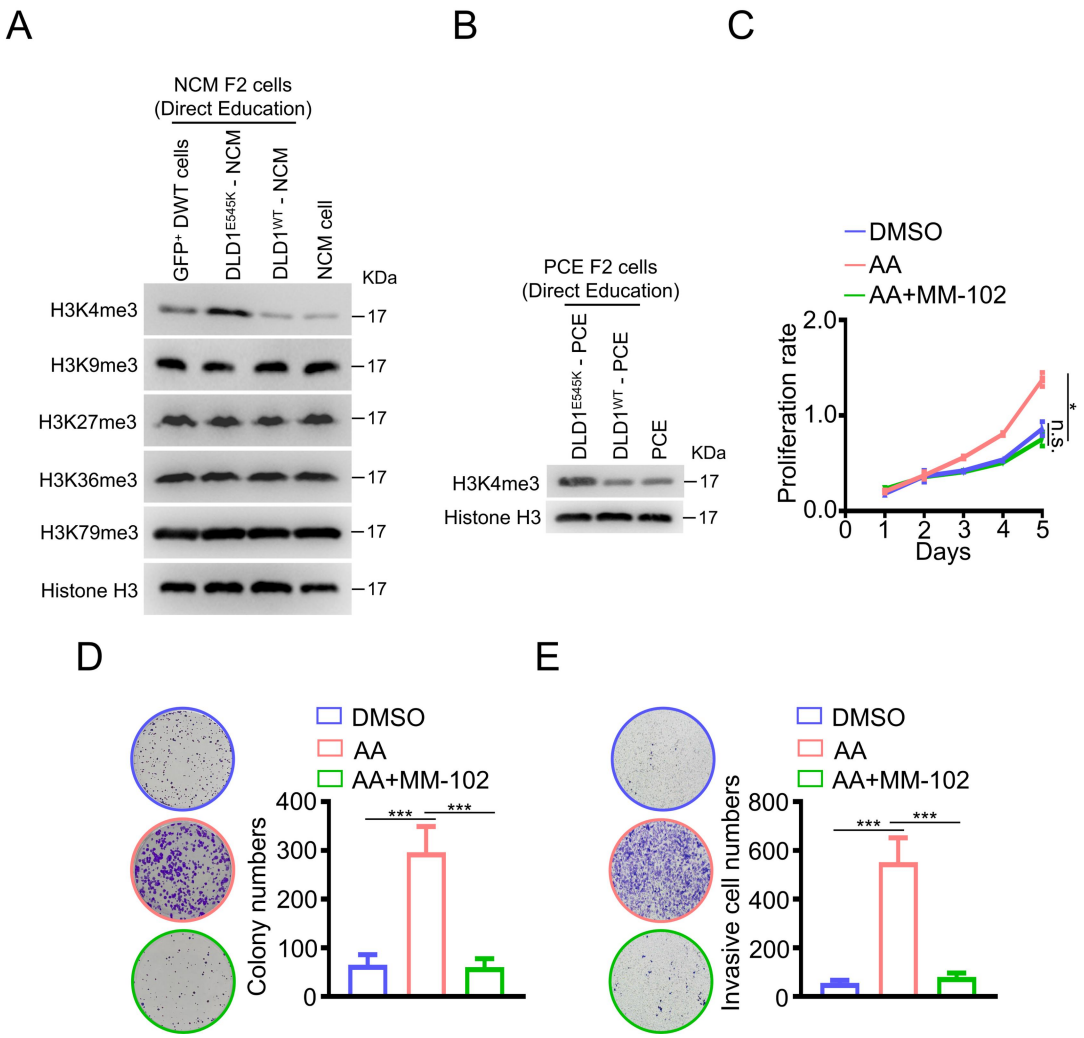

Supplemental Figure 23: Methyltransferase inhibitor MM-102 reverses AA-mediated cell proliferation, colony formation, and cell invasion in NCM460 cells (related to Fig. 5).

(A and B) Immunoblot analysis of lysates from NCM460 F2 cells and PCE F2 cells obtained from the Direct Education Model, probed with the indicated antibodies.

(C-E) *In-vitro* function including cell viability (C, means ± SEM, n = 3 biological replicates), colony forming efficiency (D, means ± SEM, n = 3 biological replicates), and cell invasive ability (E, means ± SEM, n = 3 biological replicates) in NCM460 cells treated with DMSO, 10 μM AA, or 10 μM AA plus 50 μM MM-102 was assayed. The treatment time was 48 h.

Statistical analyses, n.s., not significant; $^{*}p < 0.05$; $^{***}p < 0.001$. P-values in (C) were tested with with two-way ANOVA test. P-values in (D) and (E) were calculated with two-tailed student's t-test.

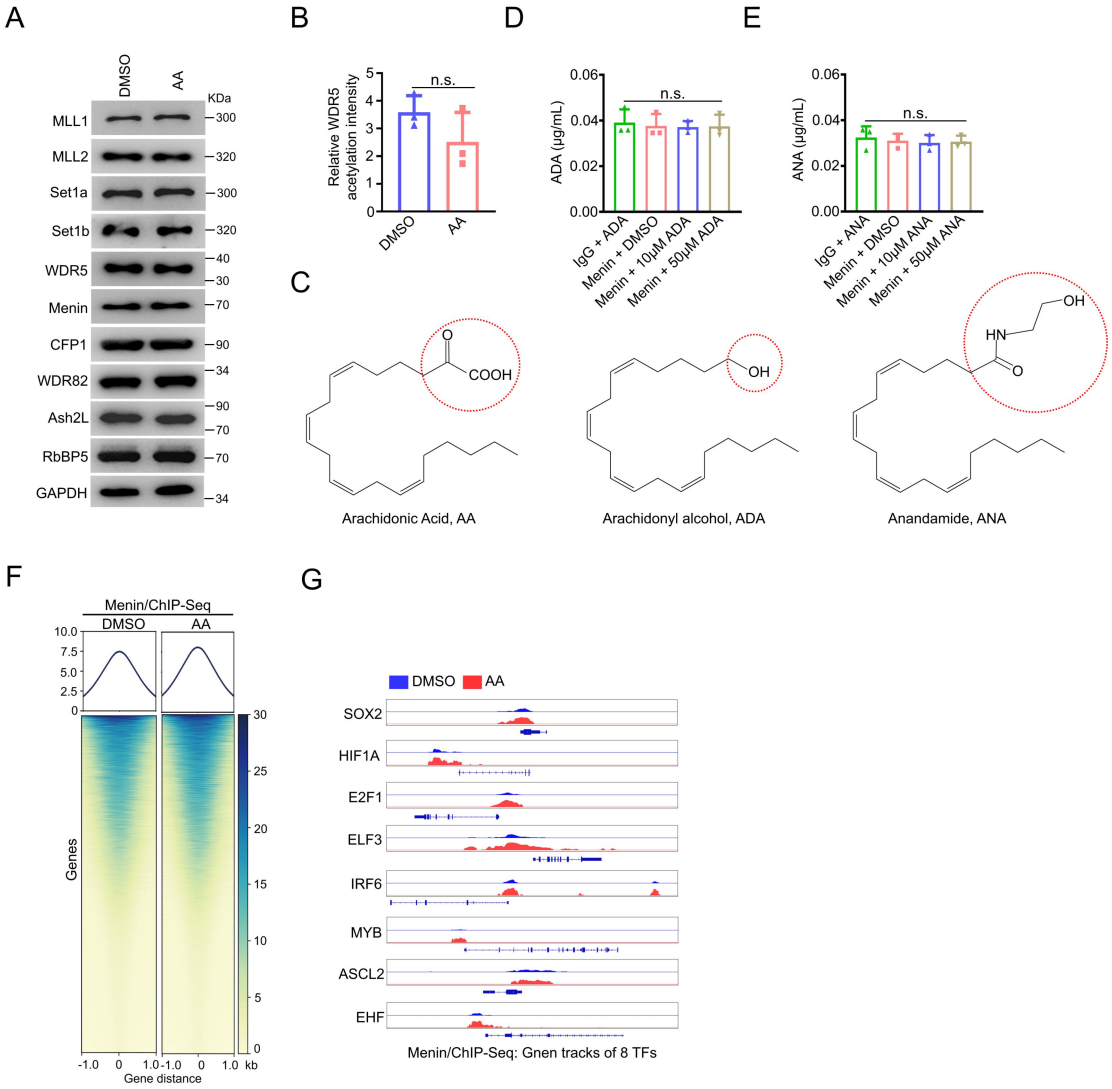

Supplemental Figure 24: AA does not impact the expression and acetylation level of Compass complex subunits; AA analogues (ADA and ANA) do not physiologically interact with Menin (related to Fig. 6).

(A) Immunoblot analysis of lysates from NCM460 cells treated with DMSO or AA, probed with the indicated antibodies.

(B) Measurement of acetylation levels of subunit proteins from the Compass complex. Detectable acetylation modifications were observed only in the WDR5 regulatory subunit protein, with no significant differences in the AA (10 μM for 48 h) treatment group compared to control (means ± SEM, n = 3 biological replicates).

(C) Chemical formulas of AA and its analogues with substituted carboxyl groups (ADA) or ethanolamine groups (ANA).

(D and E) Purified 6 × His-Menin proteins were incubated with varying amounts of

ADA or ANA. Immunoprecipitation assay was performed using anti-Menin antibody, and the immunocomplex was quantitatively assessed for ADA (D, means ± SEM, n = 3 biological replicates) or ANA (E, means ± SEM, n = 3 biological replicates) using LC-MS-based trace-level quantitation of metabolites.

(F) ChIP-seq analysis of Menin in NCM460 cells treated with DMSO or AA. NCM460 cells were treated with DMSO or 10 μM AA for 48 h. Then, cells were fixed using formaldehyde and subjected to ChIP-sequencing.

(G) Gene tracks of the 8 TFs locus with corresponding ChIP-seq coverage files using Menin antibody.

Statistical analyses, n.s., not significant. P-values in (B), (D) and (E) were calculated with two-tailed student's t-test.

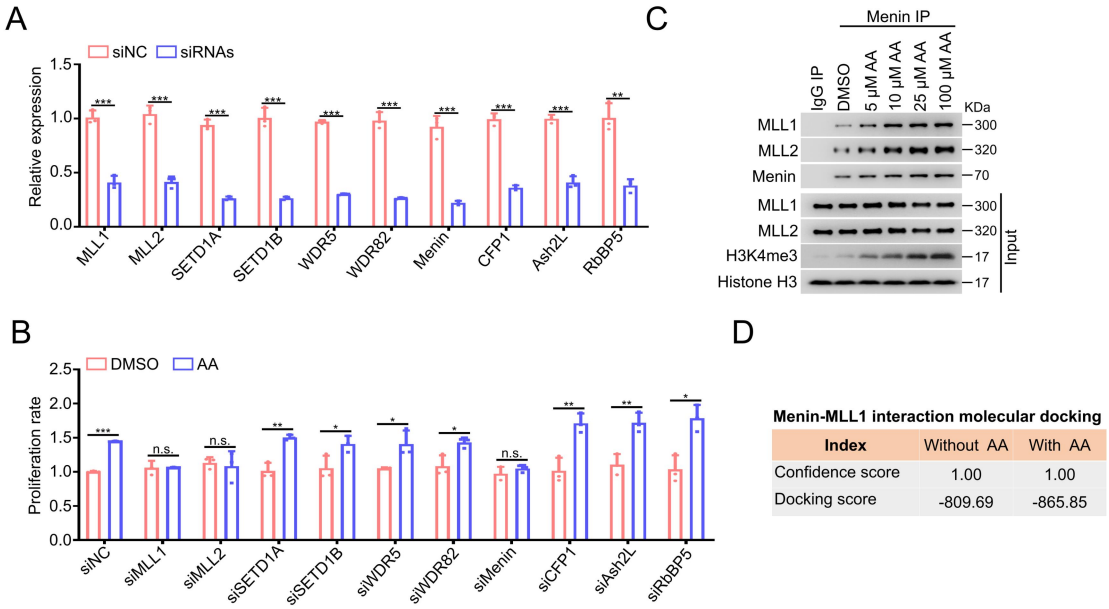

Menin-MLL1 interaction molecular docking

Index	Without AA	With AA
Confidence score	1.00	1.00
Docking score	-809.69	-865.85

Supplemental Figure 25: AA enhances the interaction between Menin and MLL1/2 (related to Fig. 6).

(A) The knock-down efficiency of MLL1, MLL2, SET1A, SET1B, RbBP5, WDR82, CFP1, Menin, WDR5, and Ash2L genes were evaluated using qPCR assay (means ± SEM, n = 3 technical replicates).

(B) NCM460 cells were transfected with scrambled siRNA (NC) or siRNAs against Compass complex subunits including MLL1, MLL2, SET1A, SET1B, RbBP5, WDR82, CFP1, Menin, WDR5, and Ash2L. Subsequently, cells were treated with DMSO or AA, and cell viability was assayed (means ± SEM, n = 3 biological replicates).

(C) PCE cells were treated with varying amounts of AA. Cells were lysed, immunoprecipitated with anti-Menin antibody, and blotted with the indicated antibodies.

(D) Docking scores of the interaction between Menin and MLL1 with or without the participation of AA.

Statistical analyses, n.s., not significant; $^{*}p < 0.05$; $^{**}p < 0.01$; $^{***}p < 0.001$. P-values in (A) and (B) were calculated with two-tailed student's t-test.

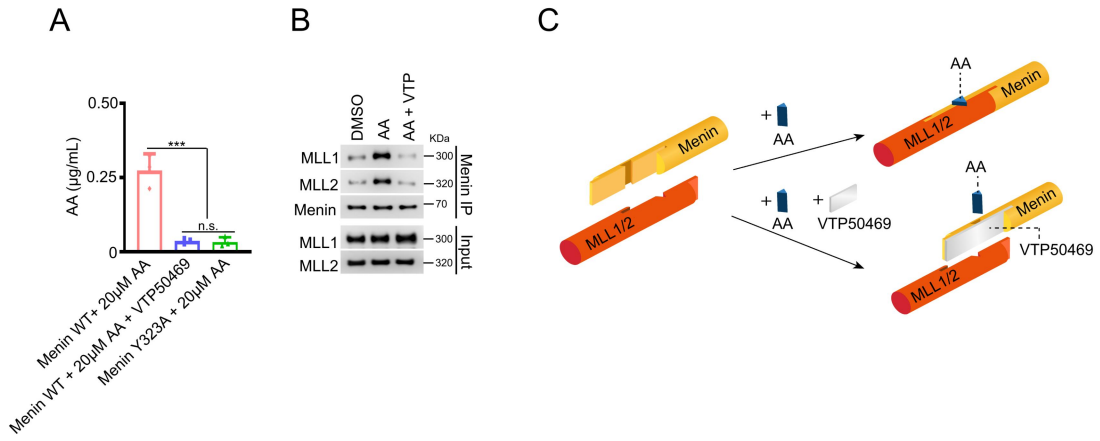

Supplemental Figure 26: VTP50469 blocks the interaction of Menin and MLL1/2 induced by AA (related to Fig. 7).

(A) Incubation of 1 μg purified 6 × His-Menin WT or Y323A mutant proteins with 10 μM AA or 100 nM VTP50469 was conducted at 37 ℃ for 6h. Then, immunoprecipitation was performed using anti-Menin antibody. Metabolites in the immunocomplex were extracted using methanol. Quantitative abundance of AA was measured using a LC-MS-based trace-level metabolite detection method (means ± SEM, n = 3 biological replicates).

(B) NCM460 cells treated with DMSO, 10 μM AA, or 10 μM AA plus 100 nM VTP50469 for 48 h. Then, the cells were lysed, immunoprecipitated with an anti-Menin antibody, and blotted with the indicated antibodies.

(C) Schematic diagram illustrating a model in which VTP50469 weakens the interaction between Menin and MLL1 triggered by AA.

Statistical analyses, n.s., not significant; $^{***}p < 0.001$. P-values in (A) were calculated with two-tailed student's t-test.

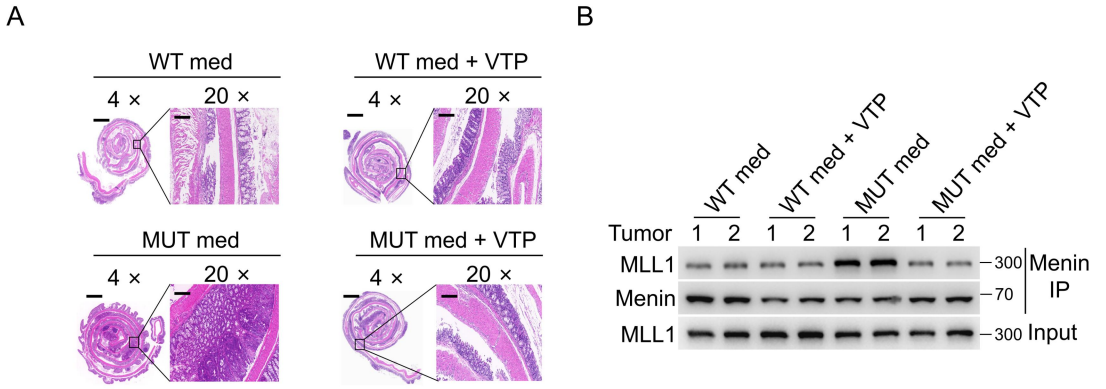

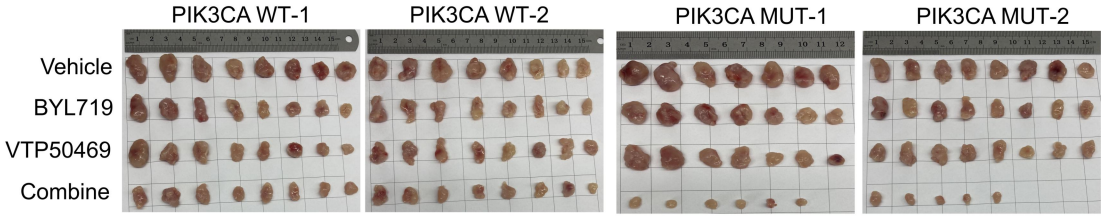

D

	PIK3CA MUT-1	PIK3CA MUT-2	PIK3CA WT-1	PIK3CA WT-2
Combine ratio	6.55	7.89	1.08	0.96
Synergy	√	√		
Additive effect			√	√
Antagonism				

Supplemental Figure 27: Supplementary results confirming the tumor repression induced by the combination of VTP50469 and Alpelisib (related to Fig. 7).

(A) Representative H&E images of colon Swiss rolls from the AOM/DSS-Induced orthotopic tumor model shown in Figure 7A. 4×: scale bar = 1000 μm; 20×: scale bar = 20 μm.

(B) Lysates of AOM/DSS-induced orthotopic tumors were immunoprecipitated with an anti-Menin antibody and blotted with the indicated antibodies.

(C) Photographs of tumors from CRC PDX models receiving drug treatment shown in Figure 7F and G.

(D) Synergistic evaluation of the drug combination on various CRC models shown in Figure 7F and G.